J|A|C|S
ARTICLES
Published on Web 09/11/2002

Determination of Multiple Torsion-Angle Constraints in U−^{13}C,^{15}N-Labeled Peptides: 3D ^{1}H−^{15}N−^{13}C−^{1}H Dipolar Chemical Shift NMR Spectroscopy in Rotating Solids

Chad M. Rienstra,[†,‡,§] Morten Hohwy,[‡,⊥] Leonard J. Mueller,[‡,∥] Christopher P. Jaroniec,[†,‡] Bernd Reif,[‡,#] and Robert G. Griffin*[,†,‡]

Contribution from the Department of Chemistry and Center for Magnetic Resonance, Francis Bitter Magnet Laboratory, Massachusetts Institute of Technology, Cambridge, Massachusetts 02139

Received June 4, 2002

Abstract: We demonstrate constraint of peptide backbone and side-chain conformation with 3D ^{1}H−^{15}N−^{13}C−^{1}H dipolar chemical shift, magic-angle spinning NMR experiments. In these experiments, polarization is transferred from ^{15}N[*i*] by ramped SPECIFIC cross polarization to the ^{13}C$^{\alpha}$[*i*], ^{13}C$^{\beta}$[*i*], and ^{13}C$^{\alpha}$[*i* − 1] resonances and evolves coherently under the correlated ^{1}H−^{15}N and ^{1}H−^{13}C dipolar couplings. The resulting set of frequency-labeled ^{15}N^{1}H−^{13}C^{1}H dipolar spectra depend strongly upon the molecular torsion angles ϕ[*i*], χ1[*i*], and ψ[*i* − 1]. To interpret the data with high precision, we considered the effects of weakly coupled protons and differential relaxation of proton coherences via an average Liouvillian theory formalism for multispin clusters and employed average Hamiltonian theory to describe the transfer of ^{15}N polarization to three coupled ^{13}C spins (^{13}C$^{\alpha}$[*i*], ^{13}C$^{\beta}$[*i*], and ^{13}C$^{\alpha}$[*i* − 1]). Degeneracies in the conformational solution space were minimized by combining data from multiple ^{15}N^{1}H−^{13}C^{1}H line shapes and analogous data from other 3D ^{1}H−^{13}C$^{\alpha}$−^{13}C$^{\beta}$−^{1}H (χ1), ^{15}N−^{13}C$^{\alpha}$−^{13}C′−^{15}N (ψ), and ^{1}H−^{15}N[*i*]−^{15}N[*i* + 1]−^{1}H (ϕ, ψ) experiments. The method is demonstrated here with studies of the uniformly ^{13}C,^{15}N-labeled solid tripeptide *N*-formyl-Met-Leu-Phe-OH, where the combined data constrains a total of eight torsion angles (three ϕ, three χ1, and two ψ): ϕ(Met) = −146°, ψ(Met) = 159°, χ1(Met) = −85°, ϕ(Leu) = −90°, ψ(Leu) = −40°, χ1(Leu) = −59°, ϕ(Phe) = −166°, and χ1(Phe) = 56°. The high sensitivity and dynamic range of the 3D experiments and the data analysis methods provided here will permit immediate application to larger peptides and proteins when sufficient resolution is available in the ^{15}N−^{13}C chemical shift correlation spectra.

I. Introduction

Applications of solid-state NMR (SSNMR) to problems in structural chemistry and biology generally rely upon systems with site-specific isotopic labels. This approach has permitted specific structural hypotheses to be addressed in a number of important problems. For example, incorporation of pairwise ^{13}C-labeled retinals into bacteriorhodopsin (bR) provided insight into the conformational changes that occur during the light-driven proton transport.[1,2] Similarly, isolated spin-$^{1}/_{2}$ nuclei in substrate (^{31}P) and inhibitor (^{13}C) were employed to constrain the structure in 5-enolpyruvylshikimate-3-phosphate synthase.[3] More recently, the antibody-dependent conformation of a 24-residue peptide was examined via ^{13}C labels in the conserved Gly-Pro-Gly-Arg motif,[4] and structures of peptides bound to surfaces were determined using pairwise labeled samples.[5,6] Such studies involving prosthetic groups, substrates and inhibitors, or target peptides lend themselves readily to site-specific isotopic labeling strategies, where a series of experiments with appropriate samples can answer outstanding questions of structure and dynamics. This very powerful approach provides precise structural constraints and will likely continue to be a preferred method to address detailed mechanistic questions.

Nevertheless, it is well known from NMR studies of proteins and nucleic acids in solution that larger numbers of constraints are required for complete structure determination.[7−10] Such a

* Corresponding author. E-mail: RGG@MIT.EDU.
† Department of Chemistry.
‡ Center for Magnetic Resonance.
§ Present address: Department of Chemistry, University of Illinois, Urbana, IL 61801.
⊥ Present address: Institute for Molecular Biology and Biophysics, ETH−Honggerberg, CH-8093 Zurich, Switzerland.
∥ Present address: Department of Chemistry, University of California, Riverside, CA 92521.
Present address: Institute for Organic Chemistry and Biochemistry, Technical University of Munich, D-85746 Garching, Germany.

(1) Creuzet, F.; McDermott, A. E.; Gebhard, R.; van der Hoef, K.; Spijker-Assink, M. B.; Herzfeld, J.; Lugtenburg, J.; Levitt, M. H.; Griffin, R. G. *Science* **1991**, *251*, 783−786.
(2) McDermott, A. E.; Creuzet, F.; Gebhard, R.; Vanderhoef, K.; Levitt, M. H.; Herzfeld, J.; Lugtenburg, J.; Griffin, R. G. *Biochemistry* **1994**, *33*, 6129−6136.
(3) McDowell, L. M.; Klug, C. A.; Beusen, D. D.; Schaefer, J. *Biochemistry* **1996**, *35*, 5395−5403.
(4) Weliky, D. P.; Bennett, A. E.; Zvi, A.; Anglister, J.; Steinbach, P. J.; Tycko, R. *Nat. Struct. Biol.* **1999**, *6*, 141−145.
(5) Long, J. R.; Dindot, J. L.; Zebroski, H.; Kiihne, S.; Clark, R. H.; Campbell, A. A.; Stayton, P. S.; Drobny, G. P. *Proc. Natl. Acad. Sci. U.S.A.* **1998**, *95*, 12083−12087.
(6) Long, J. R.; Shaw, W. J.; Slayton, P. S.; Drobny, G. P. *Biochemistry* **2001**, *40*, 15451−15455.
(7) Wüthrich, K. *NMR of Proteins and Nucleic Acids*; John Wiley and Sons: New York, 1986.

10.1021/ja020802p CCC: $22.00

quantity of data can be derived from experiments in multiple samples, and several small peptides have been studied extensively with SSNMR using this approach. Initially, a structure of the C-terminal nine residues of β-amyloid[11] was determined by measuring multiple $^{13}C^{\alpha}-^{13}C'$ distances with rotational resonance.[12,13] Other β-amyloid fragments were investigated by numerous $^{13}C'-^{13}C'$ DRAWS distance measurements[14] and by multiple quantum methods.[15] Heteronuclear distance measurements with REDOR[16] have been employed to ascertain peptide conformation, often by measuring $^{15}N-^{13}C$ distances in several different, specifically pairwise labeled samples.[17]

To improve the time- and cost-efficiency of such methodology, it would obviously be beneficial to extend the repertoire of SSNMR experiments for chemical shift assignment and structure determination of peptides and proteins with multiple ^{13}C and ^{15}N spin labels. Recently, several examples of well-resolved spectra of solid, uniformly ^{13}C,^{15}N-labeled (U-^{13}C,^{15}N) peptides and proteins have been recorded, with the aim of performing spectral assignments with dipolar recoupling techniques. We and others have analyzed 2D $^{13}C-^{13}C$ RFDR[18] and SPC-5 spectra[19] of small peptides,[20−22] and complete assignments were obtained. RFDR has also been employed for partial assignment of two proteins at high field.[23,24] Techniques for heteronuclear $^{13}C-^{15}N$ assignment experiments in peptides have been described in detail,[22,25−27] and together with $^{13}C-^{13}C$ spectra facilitated the complete backbone assignment in the 62 amino acid SH-3 domain from α-spectrin.[28] Thus, several approaches for assigning magic-angle spinning (MAS) spectra of U-^{13}C,^{15}N-labeled peptides are now available, and certainly new and improved approaches will continue to emerge.

In contrast, fewer techniques have been demonstrated for measurement of structurally important distances in uniformly labeled peptides. This is largely due to the fact that measurements of weak couplings from 3 to 6 Å distances, which provide important structural constraints, are complicated by the presence of strong couplings due to directly bonded spins. Specifically, the weak, structurally important distances exhibit dipolar couplings of <100 Hz, whereas directly bonded species exhibit dipolar couplings of ∼1−2 kHz, and the latter dominate the quantum evolution in spin clusters.[19,29] In these circumstances, broadband recoupling methods used for assignments are not suitable. Instead, accurate $^{13}C-^{13}C$ homonuclear distance measurements require the application of spectrally selective methods such as rotational resonance (R^2)[12] or semiselective approaches based on R^2 but employing additional radio frequency (rf) fields to increase their bandwidth.[30−32] Heteronuclear broadband techniques for measuring $^{13}C-^{15}N$ distances, such as REDOR,[16] suffer from similar problems in multispin systems, and several attempts have been made to modify REDOR to account for multiple $^{13}C-^{13}C$ interactions.[33−38] One of the most recent, a version of REDOR that utilizes frequency-selective Gaussian pulses, was employed to measure a total of 16 $^{13}C-^{15}N$ distances in uniformly labeled *N*-formyl-Met-Leu-Phe-OH (MLF), the sample studied here.[39] Undoubtedly, methodology for the measurement of distances in multiply labeled samples, like that for assignments, will continue to mature.

Another important approach to constraining secondary structure in solid peptides is based upon the pronounced effect of relative tensor orientations on dipolar or chemical shift line shapes. This class of molecular torsion angle experiments has flourished in recent years, and a combination of such experiments could be important in determining local secondary structures and refining complete structures to high resolution. Principles for these experiments were first demonstrated in static[40−42] and rotating solids,[43,44] where the relative orientations of dipolar and chemical shift tensors were extracted from "ridge plots" [42] or 2D rotational sideband patterns.[43,44] More recently, the strategy of measuring relative tensor orientations has been incorporated into a number of experiments for torsion angle determination from spectra of site-specifically labeled (or natural abundance) samples, under static[45,46] and MAS[47−51] conditions.

(8) Ernst, R. R.; Bodenhausen, G.; Wokaun, A. *Principles of Nuclear Magnetic Resonance in One and Two Dimensions*; Clarendon Press: Oxford, 1991; Vol. 14.
(9) Cavanagh, J.; Fairbrother, W. J.; Palmer, A. G.; Skelton, N. J. *Protein NMR Spectroscopy: Principles and Practice*; Academic Press: San Diego, 1996.
(10) Wüthrich, K. *Nat. Struct. Biol.* **1998**, *5*, 492−495.
(11) Lansbury, P. T.; Costa, P. R.; Griffiths, J. M.; Simon, E. J.; Auger, M.; Halverson, K. J.; Kocisko, D. A.; Hendsch, Z. S.; Ashburn, T. T.; Spencer, R. G. S.; Tidor, B.; Griffin, R. G. *Nat. Struct. Biol.* **1995**, *2*, 990−998.
(12) Raleigh, D. P.; Levitt, M. H.; Griffin, R. G. *Chem. Phys. Lett.* **1988**, *146*, 71−76.
(13) Levitt, M. H.; Raleigh, D. P.; Creuzet, F.; Griffin, R. G. *J. Chem. Phys.* **1990**, *92*, 6347−6364.
(14) Benzinger, T. L. S.; Gregory, D. M.; Burkoth, T. S.; Miller-Auer, H.; Lynn, D. G.; Botto, R. E.; Meredith, S. C. *Proc. Natl. Acad. Sci. U.S.A.* **1998**, *95*, 13407−13412.
(15) Antzutkin, O. N.; Balbach, J. J.; Leapman, R. D.; Rizzo, N. W.; Reed, J.; Tycko, R. *Proc. Natl. Acad. Sci. U.S.A.* **2000**, *97*, 13045−13050.
(16) Gullion, T.; Schaefer, J. *J. Magn. Reson.* **1989**, *81*, 196−200.
(17) Nishimura, K.; Naito, A.; Tuzi, S.; Saito, H.; Hashimoto, C.; Aida, M. *J. Phys. Chem. B* **1998**, *102*, 7476−7483.
(18) Bennett, A. E.; Ok, J. H.; Griffin, R. G.; Vega, S. *J. Chem. Phys.* **1992**, *96*, 8624−8627.
(19) Hohwy, M.; Rienstra, C. M.; Jaroniec, C. P.; Griffin, R. G. *J. Chem. Phys.* **1999**, *110*, 7983−7992.
(20) Bennett, A. E.; Rienstra, C. M.; Griffiths, J. M.; Zhen, W.; Lansbury, P. T., Jr.; Griffin, R. G. *J. Chem. Phys.* **1998**, *108*, 9463−9479.
(21) Zell, M. T.; Padden, B. E.; Grant, D. J. W.; Chapeau, M. C.; Prakash, I.; Munson, E. J. *J. Am. Chem. Soc.* **1999**, *121*, 1372−1378.
(22) Rienstra, C. M.; Hohwy, M.; Hong, M.; Griffin, R. G. *J. Am. Chem. Soc.* **2000**, *122*, 10979−10990.
(23) McDermott, A.; Polenova, T.; Bockmann, A.; Zilm, K. W.; Paulsen, E. K.; Martin, R. W.; Montelione, G. T. *J. Biomol. NMR* **2000**, *16*, 209−219.
(24) Pauli, J.; van Rossum, B.; Forster, H.; de Groot, H. J. M.; Oschkinat, H. *J. Magn. Reson.* **2000**, *143*, 411−416.
(25) Straus, S. K.; Bremi, T.; Ernst, R. R. *J. Biomol. NMR* **1998**, *12*, 39−50.
(26) Baldus, M.; Petkova, A. T.; Herzfeld, J. H.; Griffin, R. G. *Mol. Phys.* **1998**, *95*, 1197−1207.
(27) Hong, M. *J. Biomol. NMR* **1999**, *15*, 1−14.
(28) Pauli, J.; Baldus, M.; van Rossum, B.; de Groot, H.; Oschkinat, H. *ChemBioChem* **2001**, *2*, 101−110.
(29) Hodgkinson, P.; Emsley, L. *J. Magn. Reson.* **1999**, *139*, 46−59.
(30) Takegoshi, K.; Nomura, K.; Terao, T. *Chem. Phys. Lett.* **1995**, *232*, 424−428.
(31) Costa, P. R.; Sun, B. Q.; Griffin, R. G. *J. Am. Chem. Soc.* **1997**, *119*, 10821−10830.
(32) Takegoshi, K.; Nomura, K.; Terao, T. *J. Magn. Reson.* **1997**, *127*, 206−216.
(33) Michal, C. A.; Jelinski, L. W. *J. Am. Chem. Soc.* **1997**, *119*, 9059−9060.
(34) Gullion, T.; Pennington, C. H. *Chem. Phys. Lett.* **1998**, *290*, 88−93.
(35) Schaefer, J. *J. Magn. Reson.* **1999**, *137*, 272−275.
(36) Jaroniec, C. P.; Tounge, B. A.; Rienstra, C. M.; Herzfeld, J.; Griffin, R. G. *J. Am. Chem. Soc.* **1999**, *121*, 10237−10238.
(37) Jaroniec, C. P.; Tounge, B. A.; Rienstra, C. M.; Herzfeld, J.; Griffin, R. G. *J. Magn. Reson.* **2000**, *146*, 132−139.
(38) Liivak, O.; Zax, D. B. *J. Chem. Phys.* **2000**, *113*, 1088−1096.
(39) Jaroniec, C. P.; Tounge, B. A.; Herzfeld, J.; Griffin, R. G. *J. Am. Chem. Soc.* **2001**, *123*, 3507−3519.
(40) Stoll, M. E.; Vega, A. J.; Vaughn, R. W. *J. Chem. Phys.* **1976**, *65*, 4093−4098.
(41) Rybaczewski, E. F.; Neff, B. L.; Waugh, J. S.; Sherfinksi, J. S. *J. Chem. Phys.* **1977**, *67*, 1231−1236.
(42) Linder, M.; Höhener, A.; Ernst, R. R. *J. Chem. Phys.* **1980**, *73*, 4959−4970.
(43) Munowitz, M. G.; Griffin, R. G.; Bodenhausen, G.; Huang, T. H. *J. Am. Chem. Soc.* **1981**, *103*, 2529−2533.
(44) Munowitz, M. G.; Aue, W. P.; Griffin, R. G. *J. Chem. Phys.* **1982**, *77*, 1686.
(45) Dabbagh, G.; Weliky, D. P.; Tycko, R. *Macromolecules* **1994**, *27*, 6183−6191.
(46) Schmidt-Rohr, K. *J. Am. Chem. Soc.* **1996**, *118*, 7601−7603.
(47) Feng, X.; Lee, Y. K.; Sandström, D.; Edén, M.; Maisel, H.; Sebald, A.; Levitt, M. H. *Chem. Phys. Lett.* **1996**, *257*, 314−320.
(48) Ishii, Y.; Terao, T.; Kainosho, M. *Chem. Phys. Lett.* **1996**, *256*, 133−140.

MAS techniques that combine distance and torsion angle constraints (via relative $^{13}C'-^{13}C'$ CSA measurements) have also been successful in determining peptide secondary structure.[52−54]

The SSNMR torsion angle techniques, especially those based upon relative $^1H-^{13}C$ and $^1H-^{15}N$ dipole vector orientations, are potentially well suited for application to U-^{13}C,^{15}N-labeled peptides. In particular, the presence of additional spectator ^{13}C or ^{15}N spins does not fundamentally alter the relevant four-spin $^1H-^{15}N-^{13}C-^1H$ dynamics. Thus, 3D experiments might be designed where the dipolar modulation of each cross peak in a 2D $^{15}N-^{13}C$ chemical shift spectrum reports upon the relative orientations of the $^1H-^{15}N$ and $^1H-^{13}C$ vectors. Here we attempt to apply 3D experiments for torsion angle measurements to uniformly labeled solid molecules. To do so optimally in U-^{13}C,^{15}N samples, the following criteria should be met: (1) The experiment should be performed under conditions compatible with high resolution and sensitivity. (2) The dipolar spectra should have a large dynamic range so that a single (synchronous) dipolar dimension provides sufficient angular precision. (3) Each $^{15}N-^{13}C$ pair should be labeled according to chemical shift. (4) The data interpretation should be tractable despite the inherent multispin dynamics. We attempt to address these requirements by combining 2D $^{15}N-^{13}C$ chemical shift correlation spectroscopy with T-MREV[55] of $^1H-^{13}C$ and $^1H-^{15}N$ interactions. The experiments were performed at relatively high MAS rates for resolution and sensitivity in the directly observed ^{13}C spectra. The γ-encoded T-MREV sequence was employed to maximize the dynamic range of the dipolar evolution in a single (synchronous) dimension; reducing the dipolar portion of the experiment to one dimension permitted two dimensions of chemical shifts to be used for time-efficient frequency labeling. Thus, each $^{15}N[i]-^{13}C^{\alpha}[i]$, $^{15}N[i]-^{13}C^{\beta}[i]$, and $^{15}N-[i+1]-^{13}C^{\alpha}[i]$ pair was unambiguously identified, permitting two or three torsion angle constraints for each residue to be derived from a single 3D $^1H-^{15}N-^{13}C-^1H$ data set. To avoid the potential computational bottleneck of multispin full-matrix simulations, we describe the spin dynamics by average Hamiltonian and Liouvillian results. We include a thorough statistical analysis demonstrating that the precision of these constraints compares favorably with those measured in spin pairs.

The scheme presented here measures as many as three independent constraints per residue from $^1H-^{15}N-^{13}C-^1H$ 3D data, thereby providing a more complete description of backbone and side-chain conformation. In combination with other 3D torsion angle experiments, unambiguous solutions for the ϕ, ψ, and $\chi1$ torsion angles can be determined. We have applied this approach to the U-^{13}C,^{15}N-labeled tripeptide formyl-Met-Leu-Phe-OH and uniquely constrained eight torsion angles (three ϕ, three $\chi1$, and two ψ) from a combination of 3D experimental data. Because these schemes are compatible with experimental conditions that provide high resolution and sensitivity of solid-state NMR spectra, we expect that this approach will be directly applicable to a wide variety of U-^{13}C,^{15}N-labeled solid peptides and proteins.

II. Experimental Procedures

a. Sample Preparation. ^{15}N-Acetyl-D,L-valine was recrystallized from aqueous solution.[56] *N*-Formyl-[U-^{13}C,^{15}N]-Met-Leu-Phe-OH (MLF) was prepared as described previously,[22] using uniformly ^{13}C,^{15}N-labeled amino acids purchased from Cambridge Isotope Laboratories (CIL, Andover, MA). Other ^{15}N,$^{13}C^{\alpha}$ or U-^{15}N,^{13}C amino acids (Gly, Ala, Thr), also from CIL, were recrystallized from aqueous solution at 10−20% dilution in natural abundance material according to standard procedures.

b. NMR Spectroscopy. All NMR experiments were performed at 11.7 T (500.06, 125.7, and 50.6 MHz ^1H, ^{13}C, and ^{15}N frequencies, respectively) using a custom-designed spectrometer (courtesy of D. Ruben). The custom-designed four-channel transmission line probe used to acquire the spectra was equipped with a 4-mm spinner module (Chemagnetics-Varian, Fort Collins, CO). The probe was optimized for ^{13}C and ^{15}N observe sensitivity and long-pulse ^1H decoupling. A version of the pulse sequence shown in Figure 1 was employed for all $^1H-^{15}N-^{13}C-^1H$ experiments. Applied rf fields were typically 100 kHz on ^1H during $^{15}N-^{13}C$ cross polarization (CP), 106.8 kHz (2.34 μs $\pi/2$ pulses) during T-MREV[55] periods, and ∼85 kHz during TPPM decoupling[57] (15° total phase difference, 5.0−5.4 μs switching time), which was used in the indirect chemical shift evolution period, t_1, and acquisition, t_3. Unless indicated otherwise, the MAS rate was 8.903 kHz ± 5 Hz. CP transfers from ^1H to ^{15}N were performed with a ramp from 40 to 45 kHz on ^{15}N and a fixed amplitude field of ∼52 kHz on ^1H. CP from ^{15}N to ^{13}C was performed with ∼33 kHz constant-amplitude ^{15}N rf fields and ^{13}C rf fields ramped from 22 to 26 kHz, with the ^{13}C carrier frequency placed slightly downfield from the C^{α} resonances (70 ppm) to avoid transfer to the $^{13}C'$ resonances.[26] The ^{13}C rf amplitude ramp was optimized for efficient polarization transfer.[58] We observed no significant differences between polarization transfer achieved with linear versus tangential ramp profiles, and therefore we employed the experimentally simpler linear ramps in all experiments here. Further, the polarization transfer improved only slightly (from ∼50% to ∼55% of the direct $^1H-^{13}C$ CP polarization on the $^{13}C^{\alpha}$ signals) upon increasing the decoupling field from 100 to 120 kHz during the $^{15}N-^{13}C$ contact time, so the lower value was employed for 3D experiments.

To confirm chemical shift assignments, the T-MREV mixing time, t_2, was set to zero, and short $^{15}N-^{13}C$ CP contact times (2−4 ms) were employed to minimize transfer through space via weaker couplings (<200 Hz) to side-chain ^{13}C signals. For the 3D $^1H-^{15}N-^{13}C-^1H$ dipolar shift experiments, where direct transfers through space from N to $C^{\beta}[i]$ and $C^{\alpha}[i-1]$ were desired, the mixing times were increased to 6 ms. Because in this implementation a significant portion (∼5−10%) of the polarization transferred to each $^{13}C^{\alpha}[i]$ is from $^{15}N[i+1]$, frequency-labeling of the ^{15}N chemical shift dimension is necessary to distinguish intra- from inter-residue transfer. For the 2D $^{15}N-^{13}C$ and 3D $^1H-^{15}N-^{13}C-^1H$ experiments, 32 transients were acquired for each increment (with phase cycling according to Ruben and co-workers[59]) with a recycle delay of 2.5 s, 8 complex points (673.92 μs) in t_1, and 21 dipolar mixing time points, t_2 (for $r = 2$, sampled every 28.08 μs for the $^{13}C-^1H$ and 56.16 μs for $^{15}N-^1H$ periods). The total measurement time for each 3D $^1H-^{15}N-^{13}C-^1H$ experiment in MLF was 8 h. The analogous 2D experiment in ^{15}N-acetyl-valine (NAV), observing

(49) Hong, M.; Gross, J. D.; Griffin, R. G. *J. Phys. Chem. B* **1997**, *101*, 5869−5874.
(50) Hong, M.; Gross, J. D.; Hu, W.; Griffin, R. G. *J. Magn. Reson.* **1998**, *135*, 169−177.
(51) Hong, M.; Gross, J. D.; Rienstra, C. M.; Griffin, R. G.; Kumashiro, K. K.; Schmidt-Rohr, K. *J. Magn. Reson.* **1997**, *129*, 85−92.
(52) Tycko, R.; Weliky, D. P.; Berger, A. E. *J. Chem. Phys.* **1996**, *105*, 7915−7930.
(53) Weliky, D. P.; Tycko, R. *J. Am. Chem. Soc.* **1996**, *118*, 8487−8488.
(54) Bower, P. V.; Oyler, N.; Mehta, M. A.; Long, J. R.; Stayton, P. S.; Drobny, G. P. *J. Am. Chem. Soc.* **1999**, *121*, 8373−8375.
(55) Hohwy, M.; Jaroniec, C. P.; Reif, B.; Rienstra, C. M.; Griffin, R. G. *J. Am. Chem. Soc.* **2000**, *122*, 3218−3219.
(56) Carroll, P. J.; Stewart, P. L.; Opella, S. J. *Acta Crystallogr. C* **1990**, *46*, 243−246.
(57) Bennett, A. E.; Rienstra, C. M.; Auger, M.; Lakshmi, K. V.; Griffin, R. G. *J. Chem. Phys.* **1995**, *103*, 6951−6958.
(58) Hediger, S.; Meier, B. H.; Ernst, R. R. *Chem. Phys. Lett.* **1995**, *240*, 449−456.
(59) States, D. J.; Haberkorn, R. A.; Ruben, D. J. *J. Magn. Reson.* **1982**, *48*, 286−292.

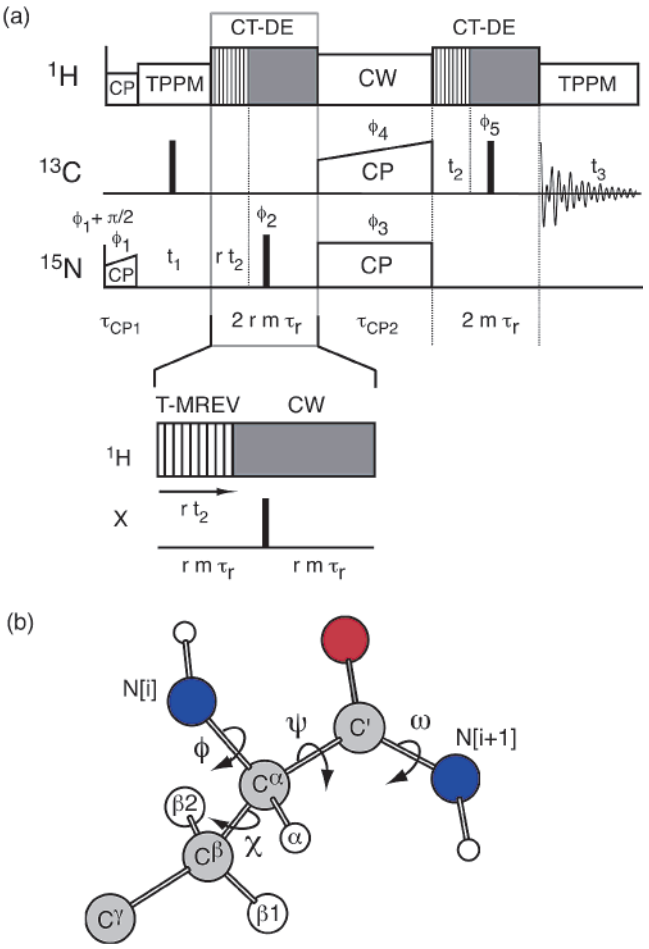

Figure 1. (a) Pulse sequence for the 3D $^1H-^{15}N-^{13}C-^1H$ dipolar chemical shift experiment to constrain ϕ, ψ, and $\chi 1$. Polarization was transferred from ^1H to ^{15}N via ramped CP, followed by ^{15}N chemical shift evolution during t_1. The period rt_2 was a constant time dipolar recoupling period, composed of an integer number of rotor periods during which T-MREV is applied to the ^1H spins.[55] Polarization was subsequently transferred from ^{15}N to ^{13}C by amplitude-ramped SPECIFIC CP,[26] and a second constant time T-MREV recoupling period, t_2, was applied to the transverse ^{13}C coherences. Signal acquisition occurred during the period t_3. The ratio of $^1H-^{15}N$ to $^1H-^{13}C$ dipolar evolution (r) was a fixed integer value, optimally 2. Narrow and wide solid rectangles represent $\pi/2$ and π pulses, respectively. Phase cycling was performed as follows, where $\phi_i = J_i(\pi/2)$: $J_1 = 1$, $J_2 =$ 1111 2222 3333 4444, $J_3 = 4$, $J_4 = 1234$, $J_5 = 2134$, and $J_{receiver} = 1234$ 3412 1234 3412. Hypercomplex data were acquired by shifting ϕ_1 according to Ruben and co-workers.[59] (b) Peptide fragment illustrating torsion angles relevant to this study. The $^{15}N^1H-^{13}C^1H$ dipolar line shapes depend strongly upon molecular geometry: $^{15}N^1H-^{13}C^{\alpha}[i]^1H$ upon ϕ, $^{15}N^1H-^{13}C^{\beta}[i]^1H$ upon ϕ and $\chi 1$, and $^{15}N[i+1]^1H-^{13}C^{\alpha}[i]^1H$ upon ψ (presuming a planar peptide bond).

the natural abundance ^{13}C signal, required 16 h (1024 transients were averaged for each of 21 data points in the dipolar domain). Fluctuations of B_1 fields were minimized by implementing pulse sequences with constant duty factor, using extra rf pulses following signal acquisition. Control spectra (CP-MAS and DCP) before and after the 2D and 3D experiments showed no significant change in signal amplitude.

The $^{15}N-^{13}C-^{13}C-^{15}N$ experiments were based upon published procedures,[60,61] with the following exceptions: (1) the SPC-5_3 sequence[19] was used to selectively excite $C^{\alpha}-C'$ DQ coherence (with a four-rotor-period excitation interval); (2) the DQ evolution period was constant time; (3) the SPI-R^3 sequence[61] was implemented with a time increment of one rotor period (83.3 μs, $\omega_r/2\pi$ 12 kHz), accomplished by alternatively adding ^{15}N rf excitation before and after the simultaneous π pulses; and (4) the SPI-R^3 sequence elements were supercycled according to the MLEV-16 scheme.[62] Proton decoupling was achieved with a 110 kHz continuous wave field during the SPC-5 and SPI-R^3 periods, and with TPPM during the acquisition.

c. Data Reduction. Cross-peak intensities were extracted using an iterative interferogram fitting routine written in FORTRAN. The frequencies, scalar couplings, and homogeneous line widths were determined from direct frequency-domain fitting of 1D ^{13}C and ^{15}N CP-MAS spectra, and these parameters were used as the initial estimates in all subsequent fitting. The $^{15}N-^{13}C$ chemical shift correlation 2D planes of the 3D experiment were fit by allowing only the cross-peak intensities to vary. This procedure resulted in precise cross-peak intensities as a function of the t_2 evolution time; the results were self-consistent with multidimensional frequency domain integration for strong signals. The calculated interferograms were less susceptible to baseline offset errors and partial overlap of strong with weak cross peaks and/or instabilities in linear prediction algorithms, which were necessary for integration but avoided in the fitting procedure. Examples are included in the Supporting Information. Cross-peak intensities determined by this method had uncertainties of $\pm 0.5\%$ ($^{15}N[i]-^{13}C^{\alpha}[i]$) to $\pm 1.5\%$ ($^{15}N[i+1]-^{13}C^{\alpha}[i]$) of the amplitude of the reference spectrum (first point in the dipolar domain).

III. Theoretical Background

a. Peptide Geometry. The orientation of all dipolar coupling tensors was defined relative to a common molecular frame, which is assumed to have its z-axis along the $C^{\alpha}-C^{\beta}$ bond. The following bond lengths were assumed: C−C, 1.52 Å; $C^{\alpha}-$N, 1.46 Å; C′−N, 1.33 Å; C−H, 1.12 Å; N−H, 1.04 Å. The C−H and N−H bond lengths are slightly longer than the distances measured in neutron diffraction experiments and correspond to a reduced effective dipolar coupling, due to small-amplitude librations, as documented in several previous dipolar chemical shift experiments.[43,44,63] Further, we assume the following bond angles: C−C−C, 113°; C′−C^{α}−N, 111°; $C^{\alpha}-$C′−N, 116°; N−$C^{\alpha}-C^{\beta}$, 113°; C−C−H, 109.5°; C^{α}−N−H, 118.6°; N−C^{α}−H; 107.6°; C^{α}−N−C′, 120°. The bond angles involving protons were obtained on the basis of the Cambridge Structural Database survey presented by Ishii et al.[64] Further details regarding the Euler angle conventions and transformations used in this analysis are available in the Supporting Information.

b. T-MREV Dipolar Evolution. All SSNMR torsion angle measurement techniques are based on the dependence of the total coherent evolution on the relative orientation of at least two tensorial interactions, usually the CSA and/or the heteronuclear dipolar coupling tensors. Because the latter provide an unambiguous correlation to the molecular frame, we focus on this case in this study. The ^1H-X (where X = ^{15}N or ^{13}C) dipolar couplings are actively recoupled during MAS by the T-MREV sequence,[55] and X chemical shifts are refocused by the π pulse during the constant time periods of the pulse sequence in Figure 1. In the quasi-static approximation, T-MREV and MAS remove the strong $^1H-^1H$ and $^{13}C-^{13}C$

(60) Feng, X.; Eden, M.; Brinkmann, A.; Luthman, H.; Eriksson, L.; Graslund, A.; Antzutkin, O. N.; Levitt, M. H. *J. Am. Chem. Soc.* **1997**, *119*, 12006−12007.
(61) Costa, P. R.; Gross, J. D.; Hong, M.; Griffin, R. G. *Chem. Phys. Lett.* **1997**, *280*, 95−103.
(62) Levitt, M. H.; Freeman, R.; Frenkiel, T. *J. Magn. Reson.* **1982**, *50*, 157−160.
(63) Roberts, J. E.; Harbison, G. S.; Munowitz, M. G.; Herzfeld, J.; Griffin, R. G. *J. Am. Chem. Soc.* **1987**, *109*, 4163.
(64) Ishii, Y.; Hirao, K.; Terao, T.; Terauchi, T.; Oba, M.; Nishiyama, K.; Kainosho, M. *Solid State Nucl. Magn. Reson.* **1998**, *11*, 169−175.

dipolar couplings, respectively, from the effective Hamiltonian, yielding[55]

$$H_{IS}^{(1)} = \sum_{i}^{n}\sum_{j}^{k}(\omega_{Ii,Sj}^{(1)} I_{i+} + \omega_{Ii,Sj}^{(-1)} I_{i-})S_{jZ} \tag{1}$$

where I and S denote the spin operators for ^{1}H and ^{13}C (or ^{15}N), and the indices i and j refer to summation over n I spins and k S spins, respectively. (Methods that do not employ the quasi-static approximation have recently been developed.[65]) We ignore the effect of the recoupled ^{1}H CSA in this treatment, since it commutes with the initial condition of transverse coherence on the low-γ spin. Each heteronuclear dipolar coupling has an orientation dependence given by

$$\omega_{Ii,Sj}^{(1)} = (\omega_{Ii,Sj}^{(-1)})^* = \kappa(b_{Ii,Sj}\sqrt{2}/4)\sin 2\beta_{ij}^{\mathrm{CR}} \tag{2}$$

where κ is the complex T-MREV scaling factor, $b_{Ii,Sj}$ is the dipolar coupling constant $-(\mu_0\hbar/4\pi)(\gamma_I\gamma_S/r_{IS}^3)$, and β_{ij}^{CR} is the Euler angle relating the common molecular frame to the rotor-fixed frame. The magnitude of κ for the 4-fold T-MREV sequence is nominally 0.485,[55] and deviates from the nominal value due to dependence upon the exact ^{1}H rf field amplitude (M. Hohwy, unpublished results). For convenience in the following, we refer to the magnitude of the effective coupling as

$$\omega_{Ii,Sj} = |\omega_{Ii,Sj}^{(1)}| = |\omega_{Ii,Sj}^{(-1)}|, \tag{3}$$

and define a phase for each interaction as

$$\Psi_{ij} = \gamma_{ij}^{\mathrm{CR}} + \lambda - \pi/2 \tag{4}$$

where $\gamma_{ij}^{\mathrm{CR}}$ is the azimuthal Euler angle relating the common molecular frame to the rotor frame, and λ is the phase of the complex scaling factor. This phase does not have an observable effect in the spectra, so the subscripts are removed from Ψ_{ij} for clarity in the following.

The pure heteronuclear Hamiltonian of eq 1 causes evolution of the initial transverse S states $|\rho(0)\rangle = \sum_j|S_{jx}\rangle$ according to $|\rho(\tau)\rangle = \sum_j|\rho_j(\tau)\rangle$. For $n = 2$,

$$\begin{aligned}|\rho_j(\tau)\rangle = \cos(\omega_{1j}\tau)\cos(\omega_{2j}\tau)|S_{jX}\rangle + \\ \sin(\omega_{1j}\tau)\cos(\omega_{2j}\tau)|2S_{jY}I_{1\Psi}\rangle \\ + \cos(\omega_{1j}\tau)\sin(\omega_{2j}\tau)|2S_{jY}I_{2\Psi}\rangle - \\ \sin(\omega_{1j}\tau)\sin(\omega_{2j}\tau)|4S_{jX}I_{1\Psi}I_{2\Psi}\rangle\end{aligned} \tag{5}$$

This expression describes the correlated dephasing effect under the influence of two protons but neglects differential relaxation of the proton coherences, which in a previous study was shown to be essential for accurate modeling of the T-MREV experimental data.[55] To account for these effects in multispin systems, we use a formulation of average Liouvillian theory (ALT),[66−68] which is also referred to in the earlier literature as the "invariant trajectory" approach,[69] to compute average relaxation in the course of a multiple-pulse experiment, where the time-dependent Hamiltonian and the relaxation superoperator are approximated as a constant superoperator. For the two-spin ($I-S$, e.g., ^{1}H−^{13}C) case, an analytical expression has been derived;[70] for larger spin clusters, we employ a semianalytical formalism by constructing the superoperator matrix of dimensionality $2^n \times 2^n$ and assigning a relaxation rate to each order of proton coherence. For example, a ^{13}C−^{1}H$_3$ cluster would be modeled by the following 8×8 matrix:

$$\frac{\mathrm{d}}{\mathrm{d}t}\begin{vmatrix} S_{jX} \\ 2S_{jY}I_{1\psi} \\ 2S_{jY}I_{2\psi} \\ 2S_{jY}I_{3\psi} \\ -4S_{jX}I_{1\psi}I_{2\psi} \\ -4S_{jX}I_{1\psi}I3_{\psi} \\ -4S_{jX}I_{2\psi}I_{3\psi} \\ -8S_{jY}I_{1\psi}I_{2\psi}I_{3\psi} \end{vmatrix} =$$

$$\begin{pmatrix} -\Gamma_1 & -\omega_{j1} & -\omega_{j2} & -\omega_{j3} & & & & \\ \omega_{j1} & -\Gamma_2 & & & -\omega_{j2} & -\omega_{j3} & & \\ \omega_{j2} & & -\Gamma_2 & & -\omega_{j1} & & -\omega_{j3} & \\ \omega_{j3} & & & -\Gamma_2 & & \omega_{j1} & -\omega_{j2} & \\ & \omega_{j2} & \omega_{j1} & & -\Gamma_3 & & & \omega_{j3} \\ & \omega_{j3} & & \omega_{j1} & & -\Gamma_3 & & -\omega_{j2} \\ & & \omega_{j3} & \omega_{j2} & & & -\Gamma_3 & -\omega_{j1} \\ & & & & \omega_{j3} & \omega_{j2} & \omega_{j1} & -\Gamma_4 \end{pmatrix} \times$$

$$\begin{vmatrix} S_{jX} \\ 2S_{jY}I_{1\psi} \\ 2S_{jY}I_{2\psi} \\ 2S_{jY}I_{3\psi} \\ -4S_{jX}I_{1\psi}I_{2\psi} \\ -4S_{jX}I_{1\psi}I_{3\psi} \\ -4S_{jX}I_{2\psi}I_{3\psi} \\ -8S_{jY}I_{1\psi}I_{2\psi}I_{3\psi} \end{vmatrix} \tag{6}$$

where Γ_j is the (average) rate of decay for coherences involving $j-1$ protons. Because the T-MREV evolution is performed in a constant time manner,

$$\Gamma_1 = 0 \tag{7a}$$

The higher order relaxation rates are computed directly via first-order ALT (see Supporting Information), assuming relaxation due to uncorrelated random fields:[71]

$$\Gamma_2 = \frac{2}{3}R_2 \tag{7b}$$

$$\Gamma_3 = \frac{9}{8}R_2 = \frac{27}{16}\Gamma_2 \tag{7c}$$

$$\Gamma_4 = \frac{77}{48}R_2 = \frac{77}{32}\Gamma_2 \tag{7d}$$

where R_2 is the rate of transverse proton coherence decay. In simulations, the relative rates for Γ_2, Γ_3, and Γ_4 are fixed by eq 7. Further, for a given set of data, all relevant proton coherences

(65) Zhao, X.; Eden, M.; Levitt, M. H. *Chem. Phys. Lett.* **2001**, *342*, 353−361.
(66) Levitt, M. H.; Dibari, L. *Phys. Rev. Lett.* **1992**, *69*, 3124−3127.
(67) Helmle, M.; Lee, Y. K.; Verdegem, P. J. E.; Feng, X.; Karlsson, T.; Lugtenburg, J.; de Groot, H. J. M.; Levitt, M. H. *J. Magn. Reson.* **1999**, *140*, 379−403.
(68) Ghose, R. *Concepts Magn. Reson.* **2000**, *12*, 152−172.
(69) Griesinger, C.; Ernst, R. R. *Chem. Phys. Lett.* **1988**, *152*, 239−247.
(70) Hohwy, M. Ph.D. Thesis, University of Aarhus: Aarhus, 2000.
(71) Kubo, A.; McDowell, C. A. *J. Chem. Soc., Faraday Trans. 1* **1988**, *84*, 3713−3730.

are assumed to have the same rate of decay. The impact of the higher order relaxation parameters on the data fitting is negligible.

This calculation requires only one numerical matrix diagonalization per crystallite, so the procedure is approximately 3 orders of magnitude faster than full Liouville matrix simulations,[70] which require matrix diagonalization in time steps that are small compared to the rotor period and rf irradiation. Such full-matrix calculations of a spin system with up to four or five spin-$^1/_2$ nuclei, subjected to a complicated train of rf pulses, significantly compromise the rate of data extraction, when considering the fact that iterative least-squares fitting is required in order to determine the optimal agreement between simulations and experiment. For example, a typical full-matrix simulation of a $^{13}C-^1H_4$ spin system with powder averaging of ~1000 crystallites requires more than 1 h on a Compaq AlphaStation running at 433 MHz. The comparable ALT requires slightly more than 1 s. This reduction in computational cost could enable very efficient data extraction for a variety of ^1H-based torsion angle experiments. For example, complete grids of simulations encompassing the torsion angle, scaling factor, and relaxation parameter spaces (many thousands of spectra), under a given set of assumptions, can be computed in a few hours using a single (433 MHz) processor.

Therefore, we aim to establish the validity of the ALT protocol for torsion angle determination by comparing the simulation methods. The ALT approximation is subjected to the usual convergence criteria for AHT (or, in general, time-dependent perturbation theory), i.e., that the interactions must be smaller than the inverse of the cycle time of the pulse sequence. Hence, the ALT result is expected to improve with higher MAS rates (as the cycle time decreases) and may be compromised in cases of large dipolar couplings and/or long relaxation times. Thus, we performed test calculations on simple spin systems employing full-matrix calculations and used the results as input for the ALT-based iterative fitting routines.

The results of one such comparison are summarized in Table 1. For weak couplings (~5 kHz), corresponding to protons not directly bonded from the X nuclei, the agreement between simulation methods is essentially quantitative (<0.3% RSMD), and values for the T-MREV scaling factor κ and relaxation parameter Γ_2 agree with the first-order theory.[55] For couplings of directly bonded $^1H-^{15}N$ pairs (~10 kHz), the agreement is slightly worse (~0.5% RMSD). For couplings of 20 kHz (Figure 2), corresponding to a directly bonded $^1H-^{13}C$ pair, the effective scaling factor κ is reduced somewhat, but in the regime of relaxation parameters typically encountered experimentally ($\Gamma_2 = \sim 3-5\ ms^{-1}$), the disagreement between simulation methods (~1%) is comparable to the noise observed in experimental spectra (vide infra). As previously demonstrated, the ALT formalism yields quantitative agreement with experimental data in the case of $^{15}N^1H$ spectra, and as shown below, experimental $^{13}C^1H$ spectra likewise can be well described by this approach.

c. Correlated Line Shapes. The overall expression for the simulated dipolar line shape must consider the dephasing of each transverse ^{15}N and ^{13}C coherence and the polarization transfer from ^{15}N to ^{13}C. We do so according to the expression where A is the relative amplitude of the observable signal as a

$$A(t_2) = D_1(rt_2) \times T(t_{CP2}) \times D_2(t_2) \quad (8)$$

Table 1. T-MREV-4 Simulation Convergence Properties[a]

full-matrix simulation		ALT simulation			
$\omega_{C,H}/2\pi$ (kHz)	R_2 (ms^{-1})	scaling (k)[b]	Γ_2 (ms^{-1})	(Γ_2/R_2)[c]	RMSD (%)
5	1.25	0.484	0.85	0.68	0.07
5	2.5	0.484	1.65	0.66	0.12
5	5.0	0.484	3.30	0.66	0.28
10	1.25	0.480	0.95	0.76	0.69
10	2.5	0.480	1.70	0.68	0.25
10	5.0	0.481	3.25	0.65	0.54
20	1.25	0.465	1.70	1.36	2.31
20	2.5	0.465	2.43	0.97	1.38
20[d]	5.0	0.466	3.53	0.71	0.80

[a] Full-matrix and average Liouvillian theory (ALT) simulation methods were compared by using the results of the full-matrix simulations as input for an iterative ALT fitting routine. The full-matrix method explicitly considered the T-MREV-4 multiple pulse sequence at $\omega_r/2\pi = 8.9$ kHz, including phenomenological transverse proton coherence decay (R_2). The ALT simulation modeled the behavior with two parameters: the dipolar scaling factor κ, and the average rate of antiphase coherence decay Γ_2. The ALT calculations were approximately 3 orders of magnitude faster than the full-matrix simulations. More details are provided in section III.b. [b] Theoretical value in the infinite MAS rate limit is 0.484. [c] Theoretical value in the infinite MAS rate limit is 0.667. [d] The simulations corresponding to these parameters are illustrated in Figure 2. The Γ_2 rate of ~3.5 ms^{-1} was the approximate value derived from most of the experiments presented in this work.

function of t_2 (as defined in Figure 1), D_1 is the dephasing of observable ^{15}N transverse coherence during the first T-MREV period (the value $|S_{1x}(rt_2)\rangle$ determined by numerically solving eq 6, where $j = 1$ refers to the ^{15}N spin), and D_2 is the dephasing of ^{13}C transverse coherence ($|S_{2x}(t_2)\rangle$). The factor $T(\tau_{CP2})$ refers to the relative polarization transfer amplitude for each crystallite. We have considered several polarization transfer models of varying complexity and will discuss their impact on the results in the context of each experimental constraint. In model I, we assume the value of $T(\tau_{CP2})$ to be constant for all crystallites (i.e., an isotropic polarization transfer, as if mediated by the scalar $^{15}N-^{13}C$ coupling). Model II assumes

$$T(\tau_{CP2}) = \sin^2(\omega_{N,}^{C1} q\tau_{CP2}) \quad (9)$$

where q is the percentage of the ramped CP amplitude period during which the ^{13}C effective field is within $\pm\omega_{N,C1}$ of the exact CP match condition. These first two models consider only one ^{13}C nucleus. If two or more ^{13}C nuclei experience $^{15}N-^{13}C$ CP conditions simulateously, the (constant-amplitude) CP spin dynamics are directly analogous to three-spin ^{13}C polarization transfer (eqs 12−15 of ref 19) with $\beta = 0$; i.e.,

$$T(\tau_{CP2}) = \sin^2\left(\frac{1}{2}\xi q\tau_{CP2}\right)[\alpha^4 + \alpha^2\gamma^2 + \alpha^2(\alpha^2 + \gamma^2)\cos(\xi q\tau_{CP2})]\frac{2}{\xi^4} \quad (10)$$

where $\xi = (\alpha^2 + \gamma^2)^{1/2}$, α is the scaled dipolar coupling of the ^{15}N to the ^{13}C destination nucleus (e.g., $\omega_{N,C\alpha}$), and γ is the coupling of ^{15}N to the competing ^{13}C spin (e.g., $\omega_{N,C\beta}$). We refer to this equation as model III.

The most elaborate computational approach (model IV) considered the evolution under the ramped SPECIFIC CP condition by extending the equations of Baldus et al.[26] to the four-spin topology N, $C^\alpha[i]$, $C^\beta[i]$, $C^\alpha[i-1]$. (The effects of the $C'[i-1]$ and $C'[i]$ spins are strictly avoided by the choice of SPECIFIC CP condition.) The ramped rf field profile on the

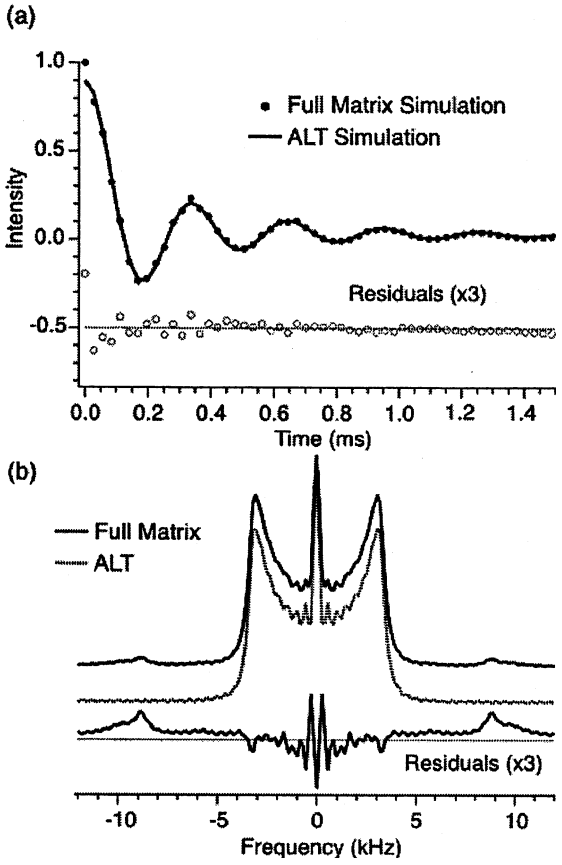

Figure 2. Simulated T-MREV $^{13}C^{1}H$ dipolar spectra, comparing the full-matrix and average Liouvillian theory (ALT) calculation methods. (a) Time-domain trajectories of one ^{13}C transverse coherence under the influence of the directly bonded ^{1}H. (b) The same data in the frequency domain. Full-matrix simulations assumed the MAS rate $\omega_r/2\pi = 8.903$ kHz, $^{13}C-^{1}H$ coupling $\omega_D = 20$ kHz, and transverse proton coherence decay rate $R_2 = 5$ ms^{-1}. The ALT simulation was fitted to the full-matrix simulation in the frequency domain, with three adjustable parameters: effective T-MREV scaling factor (κ), average proton coherence decay rate (Γ_2), and an overall amplitude scaling factor (y). These parameters are recorded in Table 1, over a range of effective dipolar couplings and relaxation rates. The ALT simulations were approximately 3 orders of magnitude faster than the full-matrix simulations.

^{13}C channel was used explicitly to calculate the effective four-spin Hamiltonian for each short time period.

d. Statistical Analysis. Statistical analysis in multidimensional parameter spaces was performed by Monte Carlo analysis.[72,73] ALT simulations were performed over a grid of possible solutions, ranging over the entire parameter space relevant to the experimental data type (e.g., ϕ for $^{15}N^{1}H-^{13}C^{\alpha}$-$[i]^{1}H$, ϕ and $\chi 1$ for $^{15}N^{1}H-^{13}C^{\beta}[i]^{1}H_2$, etc.) in $1°-2.5°$ steps, the range of relaxation parameters (Γ_2) from 0 to 8 ms^{-1} (in 0.25−0.50 ms^{-1} steps), and T-MREV scaling factors (κ) ±20% from the nominal expected value (in ∼2% steps). Construction of such grids required 12−48 h of computational time using the ALT method and was not at all feasible using full-matrix methods. The global best fit of experimental data to the grid of simulations was found and the root-mean-square deviation (RMSD) computed. A test data set was constructed by adding random noise (with a Gaussian envelope defined by the RMSD value) to the best-fit data. The best-fit parameters for the test data set were determined by comparing to the simulation grid, and the process was repeated, typically 5000−10 000 times. The numbers of solutions at each value of angle, relaxation rate, and scaling factor were tabulated, and the mean and standard error of each parameter were computed by analyzing the distribution of solutions in each bin (grouped around local minima in the RMSD curves). The overall probability of a solution (within a given local minimum) is reported as the percentage of the total Monte Carlo iterations that resulted in solutions within that region.

IV. Results and Discussion

a. $^{13}C^{1}H$ T-MREV Spectra in U-^{13}C,^{15}N-Labeled Molecules. In our implementation of T-MREV dipolar chemical shift spectroscopy, the context of U-^{13}C,^{15}N labeling requires selection of a MAS rate that avoids rotational resonance broadening conditions, as previously discussed.[22,23] The secondary impact of both dipolar and scalar $^{13}C-^{13}C$ couplings upon the $^{13}C^{1}H$ dipolar spectra is expected to be minimal because only a single ^{13}C π pulse is applied in the middle of the $^{1}H-^{13}C$ evolution period, thus avoiding inadvertent π pulse $^{13}C-^{13}C$ recoupling.[18] If one π pulse is applied per rotor period, transverse ^{13}C coherence is rapidly dephased, as in the SEDRA experiment.[74] However, one π pulse over 10 or more rotor periods has a negligible effect, except very close to R^2. Second, evolution due to the $^{13}C-^{13}C$ scalar couplings causes only a minor attenuation of the transverse ^{13}C echo. For example, with a constant time period of 1.1 ms (10 τ_r at $\tau_r/2\pi = 8.9$ kHz), the scaling of the $^{13}C^{\alpha}$ CP-MAS signal is $\cos(\pi J_1\tau)\cos(\pi J_2\tau) \approx 0.975$, for $J(C^{\alpha}-C^{\beta}) \approx 35$ Hz and $J(C^{\alpha}-C') \approx 55$ Hz. Further, all points in the dipolar dephasing trajectories are scaled by the same factor, because the experiment is at constant time and the scalar coupling Hamiltonian commutes with the recoupling Hamiltonian (in the weak coupling regime), and the system therefore behaves inhomogeneously.[75] Thus, with relatively high MAS rates, the overall effect of U-^{13}C,^{15}N-labeling upon T-MREV spectra is expected to be negligible, and we have confirmed this directly via experimental comparisons of U-^{13}C,^{15}N and natural abundance (or singly $^{13}C^{\alpha}$-labeled) amino acids Gly, Ala, and Thr (data not shown).

We have examined $^{13}C^{1}H$ T-MREV spectra at increasing MAS rates by performing experiments with a common ^{1}H rf field and altering the T-MREV symmetry number n. Spectra were simulated using the ALT method, where the adjustable fit parameters are the T-MREV scaling factor (κ), the relaxation rate (Γ_2), and an amplitude scaling factor (y), corresponding to the percentage of total intensity within the range of the frequency domain fit ($\pm\omega_r/2\pi$). Quantitative agreement between experiment and ALT simulations (Figure 3a) was achieved by including the three closest protons (H^{α}, H^{N}, and $H^{\beta 1}$; fit parameters are collected in Table 2). If only the H^{α} was considered in the simulations, the quality of the fit was poor. With the addition of a second proton (either H^{N} or $H^{\beta 1}$, with optimization of ϕ or $\chi 1$ respectively; 4 fit parameters, 61 data points), the agreement improved by a 95% confidence margin. In all cases studied thus far, exclusion of the *second* proton yielded a statistically poorer fit, with at least 85% confidence,

(72) Bevington, P. R.; Robinson, D. K. *Data reduction and error analysis for the physical sciences*, 2nd ed; McGraw-Hill: Boston, 1992.
(73) Press, W. H.; Teukolsky, S. A.; Vetterling, W. T.; Flannery, B. P. *Numerical recipes*, 2nd ed; Cambridge University Press: Cambridge, 1992.
(74) Gullion, T.; Vega, S. *Chem. Phys. Lett.* **1992**, *194*, 423−428.
(75) Maricq, M. M.; Waugh, J. S. *J. Chem. Phys.* **1979**, *70*, 3300.

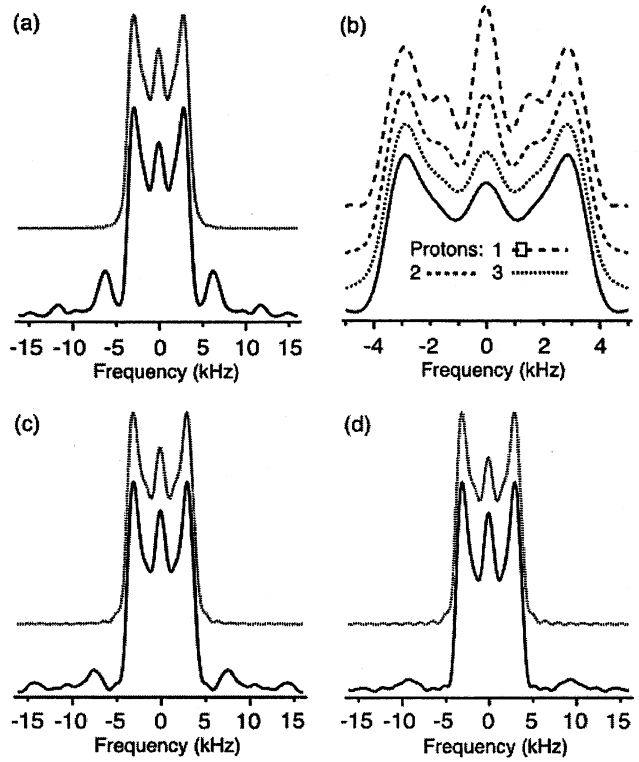

Figure 3. T-MREV dipolar $^{13}C^1H$ spectra of N-formyl-U-^{13}C,^{15}N-Met-Leu-Phe-OH, Met $^{13}C^{\alpha}$ signal, experimental (solid lines) and best-fit simulations (dotted lines). The T-MREV-*n* symmetry number (where *n* is the number of T-MREV cycles per rotor period) was modified so that all cases employed the same ^1H rf field ($\omega_{1H}/2\pi$) of 106.8 kHz (2.34 μs $\pi/2$ pulse). (a) T-MREV-6 at $\omega_r/2\pi = 5.94$ kHz, $m = 5$; (b) same experimental data as in (a), but with simulations assuming one (H^{α}), two (H^{α} and H^N), and three (H^{α}, H^N, and H^{β}) protons as indicated on the figure; (c) T-MREV-5 at $\omega_r/2\pi = 7.15$ kHz, $m = 5$; (d) T-MREV-4 at $\omega_r/2\pi = 8.90$ kHz, $m = 6$. (See Figure 1 for definition of *m*.) The simulations shown in (a), (c), and (d) here explicitly included the couplings of C^{α} to three protons (H^N, H^{α}, and $H^{\beta 1}$), with best-fit parameters recorded in Table 2. Note the reduction in cycling sideband amplitude with increasing $\omega_r/2\pi$.

Table 2. Fit Parameters for Met $^{13}C^{\alpha}-^1H$ T-MREV Spectra[a]

$\omega_r/2\pi$	no. of ^1H spins[b]	amplitude scaling (y)	dipolar scaling (κ)	relaxation rate (Γ_2, ms^{-1})	RMSD (%)
5.94	1	0.825	0.445	5.3	1.94
5.94	2	0.818	0.441	4.3	1.28
5.94	3	0.810	0.435	3.3	0.88
7.12	1	0.848	0.469	4.9	1.74
7.12	2	0.861	0.461	3.9	0.88
7.12	3	0.868	0.457	3.6	0.82
8.90	1	0.888	0.464	4.7	2.20
8.90	2	0.889	0.457	3.8	1.34
8.90	3	0.895	0.453	3.0	1.48

[a] The parameters derive from iterative fitting of experimental data, shown in Figure 3, to the ALT simulation method. [b] Number of protons simulated, in order of precedence: H^{α}, H^N, H^{β}.

based upon computation of the *F* statistic.[72] Likewise, excluding the *third* proton compromised the fit quality in the 5.94 kHz case (Figure 3b) with 80% confidence. At higher MAS rates (7.12 kHz (Figure 3c) and 8.90 kHz (Figure 3d)), excluding the third proton did not significantly degrade the quality of fit; this seems due to the fact that overall relaxation rates increase (thus damping the long-time behavior most sensitive to the distant protons) as fewer T-MREV cycles are applied per rotor period, and the quasi-static approximation (with respect to averaging the homonuclear dipolar couplings among protons) becomes less valid. Thus, for the subsequent calculations, we

Table 3. Error Analysis, MLF $^{13}C^{\alpha}$T-MREV Spectra[a]

signal	simulated protons[b]	scaling (κ)	$\sigma(\kappa)$[c]	relaxation (Γ_2, ms^{-1})	$\sigma(\Gamma_2)$[c]
Met C^{α}	2	0.4572	0.0015	3.71	0.14
Met C^{α}	3	0.4528	0.0016	3.00	0.15
Leu C^{α}	2	0.4708	0.0018	4.14	0.15
Leu C^{α}	3	0.4634	0.0017	3.13	0.15
Phe C^{α}	2	0.4681	0.0018	3.71	0.16
Phe C^{α}	3	0.4600	0.0016	2.80	0.15

[a] The Monte Carlo method[72,73] was employed to determine standard errors in the multidimensional parameter space. Additional details are provided in section III.d. [b] Order of precedence: H^{α}, H^N, $H^{\beta 1}$. [c] Standard deviation.

included at least the two protons with the strongest couplings to the low-γ nucleus, and for final simulations, we included all protons within 2.5 Å. Further, the convergence of all simulated parameters as a function of the number of simulated protons has been considered throughout this study.

The precision in determining the scaling factor (κ, Table 3) at 68% confidence ($\pm 1\sigma$) is better than $\pm 0.4\%$ (± 0.002), whether two or three protons are simulated; this corresponds to a precision of 0.001 Å in the *effective* $^{13}C-^1H$ bond length. A larger systematic shift, corresponding to -0.003 Å (-0.006 in κ), is observed between the two- and three-proton simulations. These small changes do not directly affect the torsion angle measurements, because both the $^1H-^{15}N$ and $^1H-^{13}C$ are scaled equally, and the correlated line shapes depend primarily upon the *ratio* of these couplings. Therefore, we have not attempted to determine the exact effective $^1H-^{13}C$ bond lengths, but rather we assume the value to be 1.12 Å[43,44,63] and report the experimental deviation in κ. The ensuing torsion angle experiments depend primarily upon the random uncertainty in determination of the scaling factor; i.e., ± 0.002, which corresponds to a change in $\omega_D/2\pi$ of 100 Hz, or to $\sim 1°$ in the torsion angle.

The modest decrease in the overall quality of the fits at $\omega_r/2\pi = 8.9$ kHz is, for purposes of torsion angle experiments, more than compensated for by the reduction in cycling sideband intensity, which occurs when $\omega_r/2\pi$ is much larger than the absolute scaled $^1H-^{13}C$ coupling, $\omega_{C,H}/2\pi$ (at most for any single crystallite ~ 3.7 kHz). Therefore, in the analysis of $^{13}C^1H$ T-MREV spectra of methine groups, cycling sidebands at ~ 6 kHz are not a fundamental obstacle to proper fitting with the ALT model, assuming the convergence properties are accounted for properly. However, when synchronous evolution under both the $^1H-^{15}N$ and $^1H-^{13}C$ couplings is required, as in the $^1H-^{15}N-^{13}C-^1H$ experiment, important spectral features reside in the range from ± 4 to ± 6 kHz (simulated spectra over the entire range of ϕ are included in the Supporting Information). For example, in the case where the strong $^{13}C-^1H$ and $^{15}N-^1H$ couplings are nearly collinear, the sum of the effective couplings will be ~ 5.2 kHz, or ~ 7.0 kHz if the evolution under $^{15}N-^1H$ is doubled (vide infra). Thus, the range of spectral simulation must extend to at least ± 8 kHz, and to do so rigorously with the ALT-based simulations, higher MAS rates are essential. Therefore, the torsion angle experiments have been performed at MAS rates of ~ 9 kHz, to take advantage of the fact that the ALT simulations greatly reduce computational effort for analysis of the multiple spin topologies inherent to the 3D experiment. Such MAS rates also yield high-resolution chemical shift spectra.

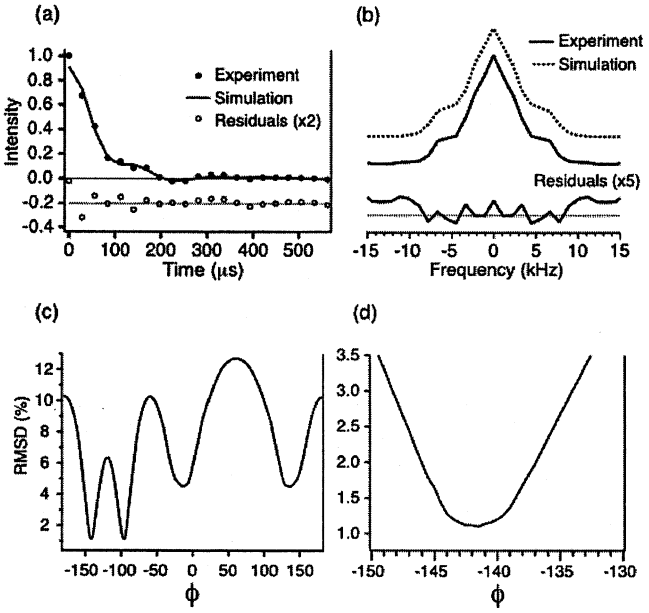

Figure 4. Experiments for the $^{15}N^1H-^{13}C^1H$ measurement of ϕ in ^{15}N-acetyl-valine. The 2D version of the pulse sequence shown in Figure 1 was used, with t_1 set to zero, since chemical shift resolution in the ^{15}N dimension was not required in this case; in t_2, 21 points were acquired with an increment of 28.08 μs, $r = 2$, and $m = 5$. The experimental data were simulated by optimizing values for the torsion angle (ϕ), the effective T-MREV scaling factor (κ), and the rate of proton coherence decay (Γ_2). (a) Time domain experimental data (filled circles) and best-fit simulation (solid line), with residuals (open circles) offset by -0.2. (b) Frequency domain experimental data (solid line) and best-fit simulation (dotted line), and residuals amplified by 5. (c) RMSD plot over the full ϕ space; at each ϕ angle (2° grid resolution), the T-MREV scaling factor κ (± 0.001) and relaxation rate Γ_2 (± 0.25 ms^{-1}) were independently optimized. (d) Expanded view of one local RMSD minimum corresponding to the crystal structure value for ϕ,[56] over which the simulations were performed with finer angular resolution. The results plotted here correspond to simulations with two protons in each dipolar evolution dimension; small shifts in the results were observed as the number of protons was varied (Table 4), with convergence achieved when all protons with 2.5 Å of each low-γ nucleus were considered in the simulation.

b. Measurement of ϕ by $^1H-^{15}N-^{13}C-^1H$ Dipolar Chemical Shift Spectroscopy. For experimental comparison with four previous studies,[49−51,64] we have performed the 2D version of the pulse sequence (Figure 1) employing ^{15}N-acetyl-valine (NAV).[56] Our implementation is conceptually similar to the relayed anisotropy correlation (RACO) experiment of Ishii and Terao.[48,64] However, in the present version, a single dipolar dimension is employed with synchronous $^1H-^{15}N$ and $^1H-^{13}C$ evolution, exploiting the high dynamic range of the γ-encoded T-MREV sequence.[55] The experimental data and ALT simulations, considering two protons (H^N, H^α) in each evolution period, are shown in Figure 4. We find a best-fit value of $\phi = -143.3$, assuming the relationship

$$\phi = \Phi_{C'-N-C^\alpha-C'} = \Phi_{H^N-N-C^\alpha-H^\alpha} + 60 \qquad (11)$$

as in previous studies.[49,51] At the resolution of the NAV crystal structure, this relationship does not hold ($\phi = \Phi_{C'-N-C^\alpha-C'} = -136.5$ and $\Phi_{H^N-N-C^\alpha-H^\alpha} = 153.4$),[56] accounting in part for the discrepancies among previously reported values. In addition, the bond angle assumptions must be considered. The directly observable parameter, the *interbond* angle $\Theta_{H^N-N-C^\alpha-H^\alpha}$ as determined in our study is 156.0 ± 0.9° ($\pm 1\sigma$, Table 4), in agreement within error to the value 153.8 ± 1.4° ($\pm 1\sigma$), reported by Ishii and co-workers.[64] Both measurements agree with, but are more precise than, the X-ray determined value, 153 ± 5° ($\pm 1\sigma$). Hong and co-workers reported ϕ directly using the assumption of eq 11, and bond angle assumptions $\Theta_{N-C^\alpha-H^\alpha} = 109.6°$ and $\Theta_{H^N-N-C^\alpha} = 120°$; thus, $\Theta_{H^N-N-C^\alpha-H^\alpha} = 162.8°$ (ref 49) and 157.5° (ref 51). Uncertainties in relative proton and heavy atom positions, and bond angles, may potentially limit the overall accuracy of proton-based torsion angle measurements. In all torsion angle fits presented here, remotely coupled protons within 2.5 Å of each X nucleus are considered to ensure convergence. Note that the addition of the third (H^β) proton to the simulation of the $^{15}N-^1H$ evolution period does not alter the result (Table 4), because this proton is more than 2.5 Å from the ^{15}N for all $\chi 1$ conformations (and in the conformation studied here, 3.3 Å). Further, the addition of the H^β in the simulation does not imply additional adjustable parameters, because the relative relaxation rates are fixed by eq 7, and the value of incidental $\chi 1$ torsion angle does not alter the results; standard geometry (e.g., $\chi 1 = 180°$) was assumed, and other $\chi 1$ conformers (e.g., $\chi 1 = 60°$ or $-60°$) were checked for completeness.

Table 4. Fit Parameters: ^{15}N-Acetyl-valine $^{15}N^1H-^{13}C^{\alpha 1}H$ Spectrum[a]

protons in $^{15}N^1H$ [b]	protons in $^{13}C^1H$ [b]	y	ϕ (°)	κ	Γ_2 (ms^{-1})	RMSD (%)
1	1	0.896	−140.4	0.493	4.7	1.2
1	2	0.906	−141.3	0.487	4.4	1.2
2	2	0.907	−142.0	0.485	4.5	1.1
2	3	0.913	−143.3	0.480	3.9	1.1
3	3	0.915	−143.3 ± 0.9	0.481 ± 0.006	3.80 ± 0.04	1.1

[a] The best-fit parameters derived from iterative fitting of the experimental data presented in Figure 4. [b] These values refer to the number of protons considered during each period of the ALT simulation. The order of precedence for the $^{15}N^1H$ period is H^N, H^α, H^β; for the $^{13}C^1H$ period, H^α, H^N, H^β.

c. Experimental Optimization. Previously a coupling amplification scheme[51] was presented for enhancing the angular precision and extending the applicable MAS rate of the original $^1H-^{15}N-^{13}C-^1H$ experiment.[49] The operational MAS range was improved with the double coupling scheme but remains somewhat limited by finite pulse width effects, and we have found ∼5 kHz to be the upper threshold for which such approaches are applicable. In addition, such coupling amplification schemes are not ideally suited for U-^{13}C,^{15}N-labeled samples because of $^{13}C-^{13}C$ SEDRA dephasing effects,[74] which may be modulated as a function of the π pulse position in the rotor period and therefore complicate analysis of $^{13}C^1H$ dipolar line shapes or sideband patterns. Because T-MREV is a recoupling technique, the effect of doubling (or arbitrarily multiplying) the evolution under the $^1H-^{15}N$ coupling relative to the $^1H-^{13}C$ coupling can be achieved without making changes to the phase cycling, pulse sequence elements, or pulse widths. Furthermore, because the variable evolution period is on the $^1H-^{15}N$ portion of the sequence, the scaling of the $t_2 = 0$ point as a function of the ratio r is essentially constant (i.e., relaxation of the transverse ^{15}N coherence is negligible over the 1−2 ms constant time period). Thus, with the T-MREV approach, it is possible to compare directly the angular sensitivity of the $r = 1$, 2, and 3 versions of the $^1H-^{15}N-^{13}C-^1H$ experiment. From ALT simulations, we expect the $r = 2$ version to have approximately twice the precision as $r = 1$ or 3.

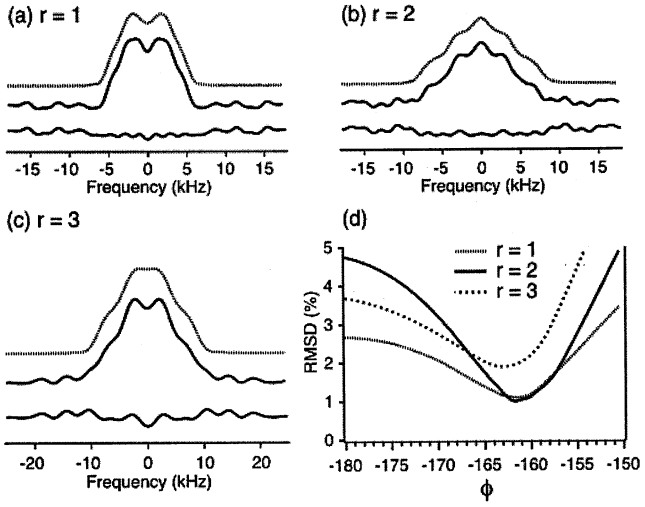

Figure 5. Effect of the relative $^1H-^{15}N$ and $^1H-^{13}C$ dipolar evolution parameter, r, on the precision of the torsion angle experiments. $^{15}N^1H-^{13}C^\alpha[i]^1H$ dipolar spectra were compared for the Phe $^{13}C^\alpha$ signal of MLF, using the 2D (t_2, t_3) version of the experiment with various ratios (r) of $^1H-^{15}N$ to $^1H-^{13}C$ T-MREV evolution (according to Figure 1). Experimental parameters were otherwise identical (T-MREV-4, $\omega_r/2\pi = 8.9$ kHz). (a) $r = 1$, experimental line shape (top), simulated line shape (middle), and residuals (bottom); (b) $r = 2$; (c) $r = 3$. (d) RMSD as a function of torsion angle for the three experiments. The simulated dipolar scaling factor and relaxation parameters were independently optimized at each torsion angle value. The measurement with $r = 2$ was approximately twice as precise as that with $r = 1$.

Experimental data (Figure 5) were extracted from the Phe $^{13}C^\alpha$ signal in a 2D version ($^{15}N^1H-^{13}C^1H,^{13}C$) ($t_1 = 0$) of the $^1H-^{15}N-^{13}C-^1H$ experiment, which is permitted in this case because the Phe $^{13}C^\alpha$ derives polarization only from its directly bonded ^{15}N neighbor. (Note that this is not the case for non-C-terminal residues, and therefore frequency labeling must be employed in those cases.) It is evident from the RMSD curves that (a) the $r = 2$ case yields the best overall agreement between experiment and simulation and (b) the slope of the RMSD curve is greatest in this case. Monte Carlo error analysis reveals that the doubling of $^1H-^{15}N$ evolution time relative to $^1H-^{13}C$ enhances angular sensitivity: for $r = 1$, $-162.0 \pm 2.6°$; for $r = 2$, $-161.9 \pm 1.2°$; for $r = 3$, $-163.2 \pm 2.3°$. All results agree within measurement error, and the $r = 2$ experiment is the most sensitive because the effective dephasing under the $^{15}N-^1H$ and $^{13}C-^1H$ couplings is matched, maximizing the interference effect as the relative tensor orientations are changed. Further, we have found through ALT simulations (not shown) that the $r = 1$ and 3 versions have greater sensitivity to numerous types of systematic errors.

d. $^{15}N-^{13}C$ Polarization Transfer Dynamics. Thus far, the discussion has been limited to cases where the identity of the ^{15}N site is unambiguous, such as in model compounds with only a single ^{15}N nucleus (e.g., ^{15}N-acetyl-valine), and in the C-terminal residue of U-^{13}C,^{15}N peptides (e.g., Phe of MLF). Because $^{15}N[i-1]-^{13}C^\alpha[i]$ distances are typically ~4 Å (vs ~1.5 Å for $^{15}N[i]-^{13}C^\alpha[i]$ and ~2.5 Å for $^{15}N[i+1]-^{13}C^\alpha[i]$), the percentage of $^{13}C^\alpha[i]$ polarization derived from the $^{15}N[i-1]$ nucleus is negligible at ~6 ms $^{15}N-^{13}C$ mixing time. Under these conditions, as was the case for the Phe residue MLF (Figure 6), no significant cross peak was observed between the Phe $^{13}C^\alpha$ and the Leu or Met ^{15}N nuclei. We have exploited this fact to perform a range of 2D control experiments, which

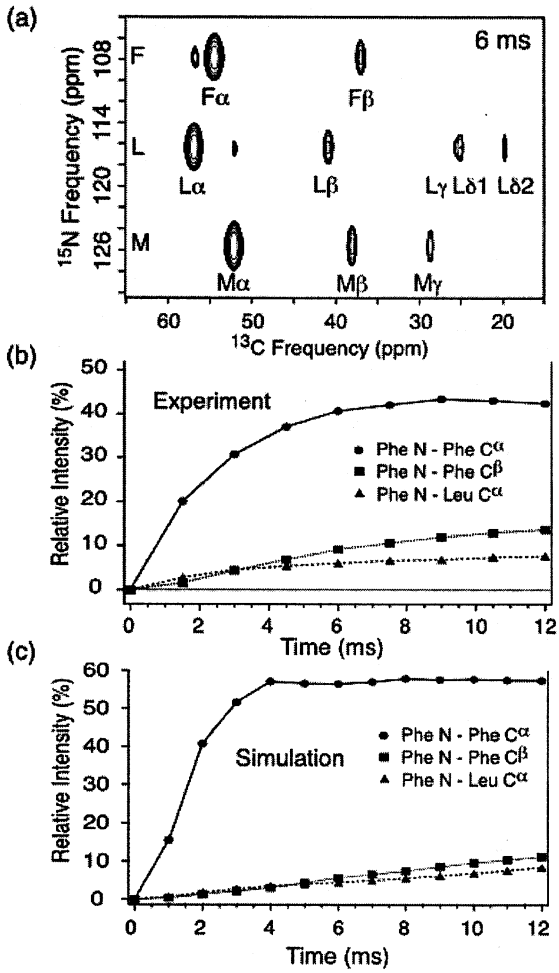

Figure 6. *N*-Formyl-U-^{13}C,^{15}N-Met-Leu-Phe-OH (MLF) 2D $^{15}N-^{13}C$ chemical shift correlation spectrum. (a) This spectrum corresponds to the first ($\omega_1/2\pi$, $\omega_3/2\pi$) plane of the 3D $^1H-^{15}N-^{13}C-^1H$ experiment (T-MREV dipolar evolution times $t_2 = 0$). $^{15}N-^{13}C$ CP mixing time was 6 ms, with a ramp of the ^{13}C field as described in the text. Each ^{15}N slice is labeled by residue type. Contours are logarithmically distributed from 3% to 60% of the largest peak intensity. (b) Experimental buildup trajectory for polarization transferred from the Phe ^{15}N resonance to the Phe $^{13}C^\alpha$, Phe $^{13}C^\beta$, and Leu $^{13}C^\alpha$ resonances. Data were extracted from a series of 2D $^{15}N-^{13}C$ experiments. The relative intensity reported for each ^{13}C resonance was normalized with respect to the signal intensity observed in the optimized 1D $^1H-^{13}C$ CP experiment. (c) Simulated trajectory for the four-spin average Hamiltonian (Phe ^{15}N, Phe $^{13}C^\alpha$, Phe $^{13}C^\beta$, Leu $^{13}C^\alpha$), assuming initial polarization on the Phe ^{15}N. The simulation explicitly considers the ramped amplitude rf applied to the ^{13}C channel and the isotropic chemical shifts.

implicitly assumed a single ^{15}N source of Phe $^{13}C^\alpha$ polarization (vide supra).

The cases of much greater general interest involve nonterminal amino acid residues in peptides, where both the source and destination spins must be frequency-labeled for accurate analysis. Note that although each ^{15}N slice of the 2D plane of Figure 6a was dominated by intra-residue cross peaks, significant cross peaks were observed between the Phe ^{15}N and Leu $^{13}C^\alpha$, and between the Leu ^{15}N and Met $^{13}C^\alpha$. In the general case, because the $^{13}C^\alpha[i]$ resonance will receive a significant portion of its polarization from both $^{15}N[i]$ and $^{15}N[i+1]$, if the ^{15}N chemical shift labeling period (t_1) is removed, the observed dipolar $^{15}N^1H-^{13}C^\alpha[i]^1H$ line shape will be an unknown admixture of intensities derived from the $^{15}N[i]$ and $^{15}N[i+1]$. In fortuitous cases, where the $^1H-^{15}N[i]-^{13}C^\alpha[i]-^1H$ and $^1H-$

$^{15}N[i+1]-^{13}C^{\alpha}[i]-^{1}H$ *interbond* angles are similar (e.g., if $\phi[i] = -120°$, $\psi[i] = +120°$, and $\omega[i] = 180°$), the resulting line shape will be essentially unchanged. However, this is not generally true, and in less favorable cases (e.g., $\phi[i] = -160°$, $\psi[i] = +120°$), errors of 5−10° in the interbond angle may arise. The magnitude of this error depends on the percentage of polarization derived from the inter-residue transfer, and therefore may be especially troublesome if U-^{15}N but selective $^{13}C^{\alpha}$ labeling is employed,[76] because the $^{13}C^{\alpha}[i]$ will derive a greater percentage of polarization from $^{15}N[i+1]$ if the $C^{\alpha}[i+1]$ site is not ^{13}C-labeled. Thus, ^{15}N frequency labeling is essential.

The $^{15}N-^{13}C$ polarization transfer function may play a significant role in the data interpretation in some instances, so we consider the dynamics in somewhat more detail here. The experimental buildup of polarization in each ^{15}N[Phe]−^{13}C cross peak as a function of $^{15}N-^{13}C$ mixing time is shown in Figure 6b, and the simulations are shown in Figure 6c. Although the simulations do not agree quantitatively with the experiments, the most important features of the buildup trajectories—such as the relative intensities of the $^{13}C^{\alpha}[i]$, $^{13}C^{\beta}[i]$, and $^{13}C^{\alpha}[i-1]$ resonances, and the buildup rates (to adequate approximation)—were reproduced. For example, the $^{13}C^{\beta}[i]$ had greater intensity at 5−10 ms contact time than the $^{13}C^{\alpha}[i-1]$ because the shape of the ^{13}C rf amplitude ramp (from low to high amplitude), and placement of the ^{13}C carrier frequency (at 70 ppm), caused the $^{15}N-^{13}C^{\beta}[i]$ SPECIFIC CP condition to be matched first, and the $^{15}N-^{13}C^{\alpha}[i-1]$ later in the ramp (at essentially the same time as the $^{15}N-^{13}C^{\alpha}[i]$ condition, resulting in a dipolar truncation effect[19,29]). Because of the direction of the amplitude ramp, therefore, exclusion of the $^{13}C^{\alpha}[i]$ and/or $^{13}C^{\alpha}[i-1]$ spins in the simulation did not affect the simulated $^{15}N-^{13}C^{\beta}[i]$ buildup curves significantly. The multispin simulation shown here was used as a standard to which simpler polarization transfer functions were compared. To estimate the upper bound on error in fitted torsion angles due to limitations of the polarization transfer model, the various $^{15}N^{1}H-^{13}C^{1}H$ line shapes were fit to these polarization transfer models, with results discussed in the context of each data type (see below).

e. Determination of ϕ and $\chi1$ from $^{15}N[i]-^{13}C^{\alpha}[i]$ and $^{15}N[i]-^{13}C^{\beta}[i]$ Cross Peaks. Presuming that each cross peak was uniquely identified by the chemical shifts, we proceeded to analyze the $^{15}N^{1}H-^{13}C^{\alpha}[i]^{1}H$ dipolar line shapes. These were relatively straightforward to fit (Table 5) because, as previously discussed,[64] the impact of the $^{15}N-^{13}C$ polarization transfer step on such ϕ measurements is minimal. The $^{15}N-^{13}C^{\alpha}$ dipole tensor is not aligned with either the $^{1}H-^{13}C$ or the $^{1}H-^{15}N$ vector, so no large correlated effects due to the polarization transfer method are expected. Further, because the majority of polarization from ^{15}N is transferred to $^{13}C^{\alpha}$, the presence of the $^{13}C^{\beta}[i]$ and $^{13}C^{\alpha}[i-1]$ spins has little impact on the $^{15}N^{1}H-^{13}C^{\alpha}[i]^{1}H$ line shape. Both of these expectations were realized in simulations and experiments. For example, Phe $^{15}N^{1}H-^{13}C^{\alpha}[i]^{1}H$ line shapes were acquired (from 2D experiments) over a range of $^{15}N-^{13}C$ contact times from 1 to 6 ms. At shorter contact times, the $^{13}C^{\alpha}$ signal intensity was correspondingly weaker, and therefore the random errors are larger ($\sigma = \sim3°$; measurement times for these 2D experiments were ca.10 min), but all results agreed within 2σ (95% confidence limits). Self-consistency was also observed in the Met and Leu $^{15}N^{1}H-^{13}C^{\alpha}[i]^{1}H$ line shapes, which were measured three times from 3D experiments with different $^{15}N-^{13}C$ CP mixing times or conditions. In simulations, the simple isotropic polarization transfer model I (see section III.c) caused shifts of only 1−2° in the ϕ results, relative to the three more elaborate models (II−IV). The simplest anisotropic polarization transfer model II produced simulations that were indistinguishable from the four-spin AHT calculations. Thus, for the $^{15}N^{1}H-^{13}C^{\alpha}[i]^{1}H$ line shape analysis, the analytical polarization transfer model II (eq 9) may be employed without significantly compromising the precision of ϕ determination; the final $^{15}N^{1}H-^{13}C^{\alpha}[i]^{1}H$ simulations, for which statistics are reported (Table 5), employed eq 9.

Table 5. MLF ϕ Measurements from $^{15}N[i]^{1}H-^{13}C^{\alpha}[i]^{1}H$ Spectra[a]

residue	solution probability (%)	$\phi \pm \sigma$ (°)	$\kappa \pm \sigma$	$\Gamma_2 \pm \sigma$ (ms^{-1})
Met	57	−149.9 ± 1.1	0.464 ± 0.008	4.4 ± 0.6
	42	−90.1 ± 1.1	0.464 ± 0.008	4.4 ± 0.6
	1	−7.1 ± 1.9	0.449 ± 0.006	3.3 ± 0.4
Leu	51	−93.6 ± 1.1	0.466 ± 0.009	5.8 ± 0.8
	49	−146.4 ± 1.0	0.467 ± 0.008	5.8 ± 0.7
Phe[b]	52	−163.1 ± 1.3	0.458 ± 0.008	5.1 ± 0.8
	39	−76.9 ± 1.4	0.458 ± 0.009	5.2 ± 0.9
	5	−44.6 ± 5.5	0.461 ± 0.011	5.2 ± 1.3
	4	161.3 ± 1.8	0.462 ± 0.009	5.1 ± 0.9

[a] Results from Monte Carlo (MC) fitting of $^{15}N^{1}H-^{13}C^{\alpha}[i]^{1}H$ spectra for each residue in MLF. The solution probability was determined by gathering sets of MC solutions around each local RMSD minimum. The overall probability for each region corresponds to the percentage of total MC solutions found within that local RMSD minimum. The means and standard errors are then calculated separately for each group of solutions. [b] The Phe constraints here are from the final 3D experiment.

(We considered whether simpler models of the spin dynamics, in particular the modeling of relaxation, would be sufficient to extract torsion angles with comparable precision. The results (Table 6) indicate that models which ignore the relaxation, or treat it as a single-exponential damping, lead to 5−10 times greater RMSD between the experiment and simulation, and therefore several-fold greater uncertainty in the determined angle. For the Phe residue data, the agreement with the simpler models was particularly poor, because this case is ∼40° from the region of optimal sensitivity for ϕ determination. Therefore, although it is possible that other methods, which employ dipolar dephasing within a single rotor period, may be adequately described without considering differential relaxation, we find these results to be less than satisfactory for the analysis of the T-MREV dipolar spectra.)

Measurements involving the $^{13}C^{\beta}$ signal likewise showed only a modest dependence on the polarization transfer dynamics, as investigated experimentally and in simulation. The deviation among the fitted ϕ and $\chi1$ angles from the $^{15}N^{1}H-^{13}C^{\beta}[i]^{1}H$ spectra, using models II−IV, was less than 2° (with no consistent trends), whereas model I differed by 3−5° in some regions of the (ϕ, $\chi1$) space. Thus, as long as the fundamental anisotropic nature of the $^{15}N-^{13}C^{\beta}[i]$ polarization transfer was considered, systematic errors were <2°, smaller than the random errors reported in Table 7; we again used polarization transfer model II for the final simulations over the entire conformational space. The Phe $^{15}N^{1}H-^{13}C^{\beta}[i]^{1}H_2$ line shape (Figure 7) depends on the extent to which the $^{13}C^{\beta}-^{1}H^{\beta1}$ and $^{13}C^{\beta}-^{1}H^{\beta2}$ vectors deviate from the plane defined by the ^{15}N, $^{1}H^{N}$, and $^{13}C^{\beta}$ nuclei, or more specifically, the $^{1}H^{N}-^{15}N-^{13}C^{\beta}-^{1}H^{\beta1}$ and $^{1}H^{N}-^{15}N-^{13}C^{\beta}-^{1}H^{\beta2}$ interbond angles (e.g., eqs 10 and 11). Because these

(76) Hong, M. *J. Magn. Reson.* **1999**, *139*, 389−401.

Table 6. Alternate Simulation Methods for MLF $^{15}N[i]^1H-^{13}C^\alpha[i]^1H$ Spectra[a]

residue	single proton, no relaxation[b]	two protons, no relaxation	two protons, single-exponential relaxation[c]	full differential relaxation model[d]
Met	$-155.4 \pm 7.8°$	$-154.4 \pm 7.0°$	$-149.2 \pm 5.3°$	$-149.9 \pm 1.1°$
Leu	$-84.8 \pm 7.1°$	$-87.5 \pm 6.3°$	$-90.7 \pm 4.5°$	$-93.6 \pm 1.1°$
Phe[b]	$-164.4 \pm 18.0°$	$-162.9 \pm 16.5°$	$-163.8 \pm 9.8°$	$-163.1 \pm 1.3°$

[a] Results from Monte Carlo (MC) fitting of $^{15}N^1H-^{13}C^\alpha[i]^1H$ spectra for each residue in MLF. The best solution near one local minimum was studied in detail. Alternate simulation methods were applied. Models ignoring relaxation, or treating it in a single-exponential fashion, resulted in close to an order of magnitude greater RMSD between experiment and simulation, and the uncertainties noted here. [b] The influence of only the directly bonded proton was included in the spin dynamics, and eq 5 was used. [c] Equivalent to using eq 6 with $\Gamma_1 = \Gamma_2 = \Gamma_3$, allowing the value to vary to find the solution, locally optimized for ϕ and globally optimized for scaling and relaxation parameters. [d] Other fit parameters are presented in Table 5.

Table 7. MLF ϕ, $\chi1$ Measurements from $^{15}N^1H-^{13}C^\beta[i]^1H_2$ Spectra[a]

residue[b]	assumed ϕ (°)	probability	$\chi1 \pm \sigma$ (°)
Met	−150	>99%	-81.5 ± 7.3[c]
Leu	−94	88%	-58.9 ± 1.9
		10%	24.3 ± 3.9
		1%	108.5 ± 5.0
		1%	168.3 ± 4.2
Phe	−163	>99%	69.0 ± 6.2[c]

[a] Results from Monte Carlo (MC) fitting of $^{15}N^1H-^{13}C^\beta[i]^1H_2$ spectra for each residue in MLF are summarized by assuming a value for ϕ (known from the combination of this and other studies to be near the correct value), and calculating the probability and uncertainty for the $\chi1$ value. As shown in Figure 7 (for Phe), the solution space is in general two-dimensional ($f(\phi,\chi1)$), so for complete peptide structure calculations the coupled solution space is explicitly considered. [b] Dipolar $^{15}N^1H-^{13}C^\beta[i]^1H_2$ spectra for the Met and Leu residues are included in the Supporting Information. [c] In these regions, the relevant *interbond* angles show stronger dependence upon ϕ than $\chi1$.

interbond angles depend on both ϕ and $\chi1$, multiple solutions are possible in the (ϕ, $\chi1$) parameter space. For example, in the Phe residue of MLF, the nearly degenerate solutions were found near (ϕ, $\chi1$) = (−165°, 70°), (−70°, 180°), or (50°, −60°); in each case, one of the relevant interbond angles is ∼120° (or ∼60°), and the other is ∼130° (or ∼50°). Similar sets of multiple solutions were observed for the other residues, and these will be discussed further below.

f. Determination of ψ from $^{15}N[i+1]-^{13}C^\alpha[i]$ Cross Peaks. The measurement of ψ from the $^{15}N[i+1]^1H-^{13}C^\alpha[i]^1H$ line shapes presents a challenging case, because a relatively small percentage of the $^{15}N[i+1]$ polarization is transferred to the $^{13}C^\alpha[i]$ in the course of the ramped SPECIFIC CP conditions used in this study. We have found that, at minimum, the strong, competing $^{15}N[i+1]-^{13}C^\alpha[i+1]$ coupling must be considered explicitly, via a three-spin ($^{15}N[i+1]$, $^{13}C^\alpha[i+1]$, $^{13}C^\alpha[i]$) AHT calculation model III (eq 10), to account for the dipolar truncation effect[19,29] that results from the small chemical shift differences among $^{13}C^\alpha$ nuclei in this case (implying that both spins are matched to the CP condition at the same point in the amplitude ramp). The simpler models I and II yielded changes in the fitted $\psi[i]$ angle shifts by several degrees, relative to model III. However, models III and IV showed very good agreement (<2° deviation), and whether the $^{13}C^\beta[i]$ spin was or was not included resulted in no significant change in the $\psi[i]$ result (because only ∼10−15% of the ^{15}N polarization is transferred to this $^{13}C^\beta$). Furthermore, relatively large changes in the model IV simulation parameters (±50% in amplitude ramp size, ±50% in effective mixing time τ', and ±10 ppm in ^{13}C chemical shifts) yielded only fraction of degree changes in the torsion angle near the global minimum solution. Therefore, we conclude that the systematic errors due to polarization transfer dynamics in the present study were comparable to or less than the random errors (Table 8) only when the slightly more involved models were employed; we used model III for final calculations. For comparison with an established method, we also performed the $^{15}N-^{13}C-^{13}C-^{15}N$ ψ experiment,[60,61] to be discussed further in section IV.g.

The ψ values determined from the $^{15}N[i+1]^1H-^{13}C^\alpha[i]^1H$ spectra were the least precise of those extracted from the 3D experiments in this study. To enhance the precision, greater signal intensity and reduced uncertainty about the polarization transfer function would be desirable. A more efficient $^{15}N-[i+1]-^{13}C^\alpha[i]$ polarization transfer process could be realized

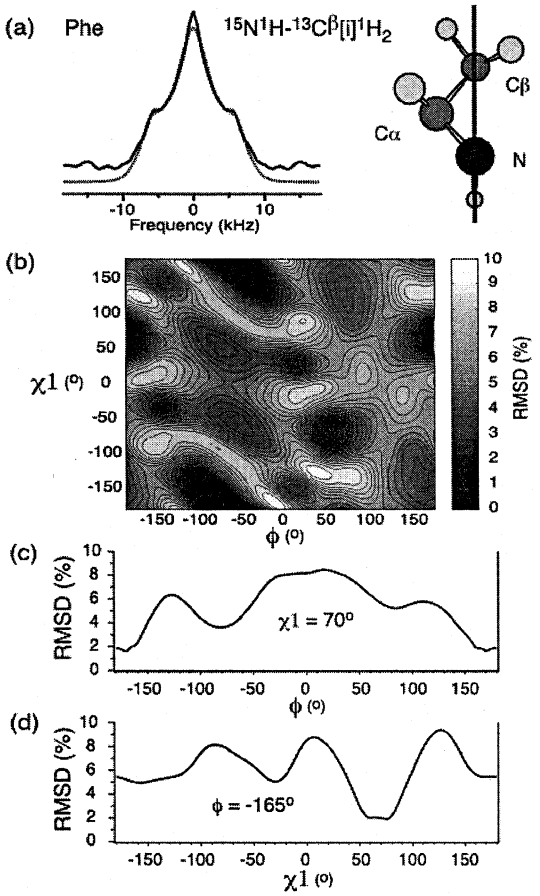

Figure 7. Measurement of ϕ and $\chi1$ for Phe in MLF, via the $^{15}N^1H-^{13}C^\beta-[i]^1H_2$ spectrum. (a) Experimental (solid line) and simulated (dotted line) dipolar line shapes, and ball-and-stick model of a conformation near (ϕ, $\chi1$) = (−165°, 70°) consistent with the best-fit results. A plane is drawn along the H^N-N-C^β nuclei. The spectra are sensitive to the deviation of the $^{13}C^\beta-^1H^{\beta1}$ and $^{13}C^\beta-H^{\beta2}$ vectors from this plane. (b) RMSD contour plot comparing the experimental spectrum with simulations as a function of ϕ and $\chi1$. The dark regions correspond to nearly degenerate local minima. As discussed in the text, only one solution is consistent with other torsion angle measurements of ϕ and $\chi1$. (c) RMSD as a function of ϕ assuming $\chi1 = 70°$. (d) RMSD as a function of $\chi1$ assuming $\phi = -165°$.

Table 8. MLF ψ Measurements from $^{15}N-^{13}C-^{13}C-^{15}N$ and $^{15}N[i+1]^1H-^{13}C^{\alpha}[i]^1H$ Spectra[a]

residue	experiment	probability[b] (%)	$\psi \pm \sigma$ (°)
Met	$^{15}N-^{13}C-^{13}C-^{15}N$	100	$\pm 156.6 \pm 0.6$
Met	$^1H-^{15}N[i+1]-^{13}C-^1H$	35	161.0 ± 3.4
		19	107.5 ± 17.2
		17	150.8 ± 9.1
		13	78.4 ± 4.8
		10	-9.5 ± 7.8
		5	23.6 ± 10.7
Leu	$^{15}N-^{13}C-^{13}C-^{15}N$	55	$\pm 90.9 \pm 3.8$
		30	$\pm 119.9 \pm 3.2$
		11	$\pm 65.0 \pm 5.1$
		4	$\pm 45.2 \pm 3.7$
Leu	$^1H-^{15}N[i+1]-13C-^1H$	46	-69.6 ± 4.4
		42	-51.2 ± 4.2
		7	58.6 ± 10.0
		6	-178.2 ± 6.8

[a] The results of all possible ψ solutions are presented. The Met ψ value was found to be near a region of high sensitivity for the $^{15}N-^{13}C-^{13}C-^{15}N$ experiment; the $^{15}N[i+1]^1H-^{13}C^{\alpha}[i]^1H$ data help to break remaining degeneracy from the mirror plane ($\pm\psi$) symmetry. In contrast, the Leu $^{15}N-^{13}C-^{13}C-^{15}N$ experiment yielded a highly ambiguous result (eight possible solutions); the $^{15}N[i+1]^1H-^{13}C^{\alpha}[i]^1H$ data were consistent with only three of those solutions (−65°, −45°, +65°). [b] Probability refers to the percentage of all Monte Carlo iterations that fell within the given local minimum.

by mediating the transfer in two steps, for example, from $^{15}N[i+1]$ to $^{13}C'[i]$ by SPECIFIC CP and then from $^{13}C'[i]$ to $^{13}C^{\alpha}[i]$ by SPC-5, as previously demonstrated,[22] or adiabatic R2T-type experiments.[31,77] Likewise for the $^{15}N^1H-^{13}C^{\beta}[i]^1H_2$ measurement, although the precision was quite good in the examples studied here, greater sensitivity could be derived from a two-step transfer through the $^{13}C^{\alpha}[i]$, based on experiments employing SPECIFIC CP in combination with HORROR[28] or DREAM[78] conditions in a band-selective manner.[28] In these scenarios, the overall polarization transfer dynamics would be dominated by two strong couplings with well-defined orientations. This strategy would likely increase the overall polarization transfer efficiency and promote compatibility with experiments of higher dimensionality utilizing narrow indirect chemical shift bandwidths (e.g., 3D $^{15}N[i]-^{13}C^{\alpha}[i]-^{13}C^{\beta}[i]$ or $^{15}N[i+1]-^{13}C'[i]-^{13}C^{\alpha}[i]$).

g. Self-Consistency of Multiple Torsion Angle Measurements. As a rigorous test of overall torsion angle measurement accuracy, we consider whether the results of several constraints are self-consistent. As described above, for the Phe residue in MLF, fits of the $^{15}N^1H-^{13}C^{\beta}[i]^1H_2$ line shape produced nearly degenerate solutions near (ϕ, $\chi1$) = (−165°, 70°), (−70°, 180°), or (50°, −60°). Only the (ϕ, $\chi1$) = (−165°, 70°) solution is consistent with the ϕ measurement from $^{15}N^1H-^{13}C^{\alpha}[i]^1H$ (Table 5) and the $\chi1$ measurement from $^{13}C^{\alpha}[i]^1H-^{13}C^{\beta}[i]^1H_2$ (68.0 ± 3.5° or 52.4 ± 3.9°, to be presented elsewhere). Likewise, the (ϕ, $\chi1$) best-fit parameters for Met and Leu $^{15}N^1H-^{13}C^{\beta}[i]^1H_2$ spectra (Table 7) are consistent with pairs of $^1H^N-^{15}N-^{13}C^{\beta}-^1H^{\beta}$ interbond angles (100° or 80°, and 40° or 140° for Met; 125° or 55°, and 30° or 150° for Leu) allowed by several (ϕ, $\chi1$) conformations, only one of which for each residue agrees with all of the complementary data. In most cases studied so far, the triangulation of molecular fragments by this approach would remain unambiguous (to 95% certainty), even if the individual experiments were 2−3 times less precise, because of the extent to which the data are complementary.

Invoking a similar strategy for the ψ measurement, we have performed the $^{15}N-^{13}C-^{13}C-^{15}N$ experiment[60,61] as an additional constraint (Figure 8). As is well known from previous studies, the $^{15}N-^{13}C-^{13}C-^{15}N$ experiment is exquisitely sensitive in the β-sheet region $|\psi| > 140°$, but ambiguous for $|\psi| < 120°$. The inherent degeneracy in this region is exacerbated by the fact that the $^{15}N-^{13}C$ recoupling portion of this experiment is not γ-encoded, leading to a relatively large covariance between dipolar scaling factor and torsion angle. Thus, the Leu $^{15}N-^{13}C-^{13}C-^{15}N$ measurement had four possible ψ solutions on each side of the mirror plane (Figure 8 and Table 8). Of the eight total solutions, only three (near −65°, −45°, and 60°) are consistent with the complementary $^{15}N[i+1]^1H-^{13}C^{\alpha}[i]^1H$ data. The remaining ambiguity was eliminated by addition of $^{15}N[i]^1H-^{15}N[i+1]^1H$ and frequency-selective REDOR data.[39,79] Thus, an unambiguous result was found despite the degeneracy of the $^{15}N-^{13}C-^{13}C-^{15}N$ experiment. The Met case provides a different example, where the $^{15}N-^{13}C-^{13}C-^{15}N$ data were fit with very high precision ($\psi = \pm 156.6 \pm 0.6°$) but, as with most torsion angle measurements, possessed a mirror-plane degenerate solution. The inclusion of $^{15}N[i+1]^1H-^{13}C^{\alpha}[i]^1H$ data clarified the solution, despite the relatively poor quality of fit in this case. Monte Carlo simulations indicate that the 161.0 ± 3.4° solution was most probable; the solution near −155° was half as probable. Again, the inclusion of $^{15}N[i]^1H-^{15}N[i+1]^1H$ data (with restrictions on ϕ from $^{15}N^1H-^{13}C^{\alpha}[i]^1H$) gave a single solution. The $^{15}N[i]^1H-^{15}N[i+1]^1H$ data alone are consistent with two rings of solutions in the (ϕ, ψ) conformational space; the data from the present work in each case unambiguously (>5 σ) eliminate one ring and extract a cross section from the other as the final solution. Thus, in MLF we have two examples of ψ measurements, in which relatively insensitive experiments help to break the 2- or greater-fold degeneracy of very precise solutions from other experiments. Recently, a new type of torsion angle experiment was introduced, involving the evolution of triple-quantum ^{13}C coherences, to break the mirror-plane symmetry in the ψ measurement.[80] Unfortunately, the extent to which the symmetry is broken, relative to the double-quantum $^{15}N-^{13}C-^{13}C-^{15}N$ experiment, is relatively small (∼9°) and, for geometries other than β-sheet, will possibly be within the random error of the measurement. In contrast, when experiments involving different sets of nuclei are combined, optimal regions of the solution space are shifted by 60° or 120°. Specifically in the example presented here, the $^{15}N-^{13}C-^{13}C-^{15}N$ experiment is optimal near $\psi = 180°$, whereas the $^{15}N[i+1]^1H-^{13}C^{\alpha}[i]^1H$ is optimal near $\psi = +120°$; the $^{15}N[i]^1H-^{15}N[i+1]^1H$ has highly sensitive regions near (ϕ, ψ) = (−50°, −60°), (60°, −70°), and (±180°, ±180°).

Within the single conformational space, deviations among the various experiments were usually ∼5° or less. At this level of precision, assumptions made about bond angles involving protons, and the extent to which the H^N may deviate from the plane of the peptide bond, are likely to be significant; fortuitously, these errors tend to contribute to each experimental measurement in a systematically different way. Therefore, the

(77) Verel, R.; Baldus, M.; Nijman, M.; van Os, J. W. M.; Meier, B. H. *Chem. Phys. Lett.* **1997**, *280*, 31−39.
(78) Verel, R.; Baldus, M.; Ernst, M.; Meier, B. H. *Chem. Phys. Lett.* **1998**, *287*, 421−428.
(79) Reif, B.; Hohwy, M.; Jaroniec, C. P.; Rienstra, C. M.; Griffin, R. G. *J. Magn. Reson.* **2000**, *145*, 132−141.
(80) Eden, M.; Brinkmann, A.; Luthman, H.; Eriksson, L.; Levitt, M. H. *J. Magn. Reson.* **2000**, *144*, 266−279.

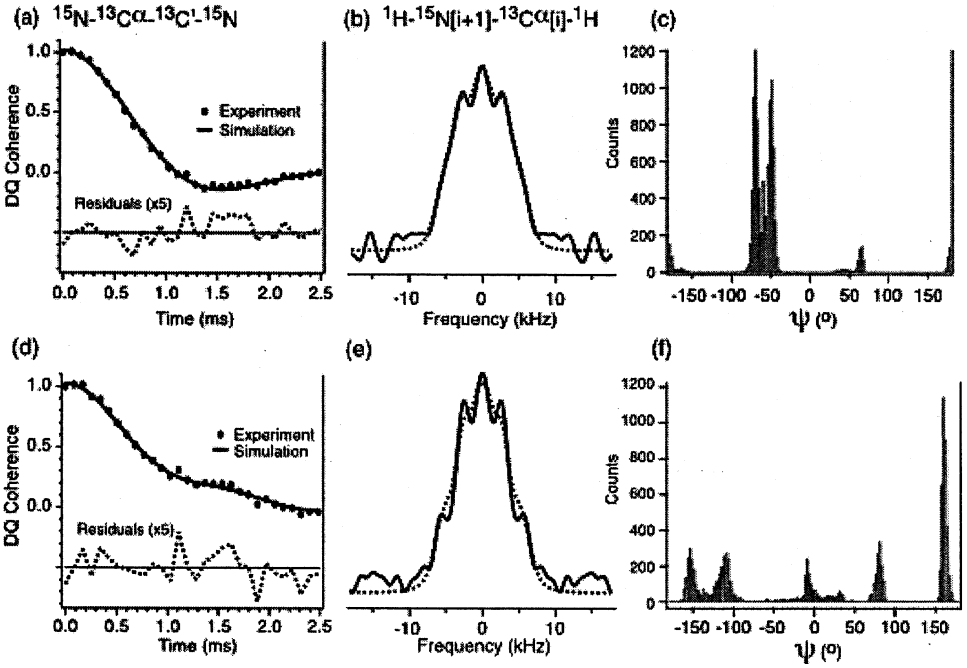

Figure 8. Measurements of ψ angles in MLF. (a) $^{15}N-^{13}C-^{13}C-^{15}N$ experimental data for the Leu $^{13}C'-^{13}C^{\alpha}$ DQ coherence, and best-fit simulations as a function of Leu ψ. (b) $^{15}N[i+1]^1H-^{13}C^{\alpha}[i]^1H$ experimental spectrum (solid line) and best-fit simulation (dotted line) for Leu. (c) Distribution of best-fit simulations of $^{15}N^1H-^{13}C^1H$ spectra as a function of Leu ψ, resulting from 10 000 iterations of Monte Carlo simulations as described in the text. (d−f) The corresponding spectra and simulations for measurement of Met ψ. The self-consistency of the various measurements is discussed in the text.

Table 9. Summary of ϕ, ψ, and $\chi1$ Torsion Angles Determined in MLF[a]

residue	angle	value	experiments[b]	coupled dependence[c]	ref
Met	ϕ	−146	H−N−C^{α}−H		*d*
			H−N−C^{β}−H_2	$\chi1$	*d*
			H−N−N[$i+1$]−H	ψ, ω	*e*
Met	ψ	159	N−C−C−N		*d*
			H−N[$i+1$]−C^{α}−H	ω	*d*
			H−N−N[$i+1$]−H	ϕ, ω	*e*
			Met(N)−Leu(C^{β})	ω, ϕ(Leu)	*f*
Met	$\chi1$	−85	H−C^{α}−C^{β}−H_2		*g*
			H−N−C^{β}−H_2	ϕ	*d*
			Met(N)−Met(C^{γ})		*f*
			H−C^{α}−C^{γ}−H_2	$\chi2$	*g*
Leu	ϕ	−90	H−N−C^{α}−H		*d*
			H−N−C^{β}−H_2	$\chi1$	*d*
			H−N−N[$i+1$]−H	ψ, ω	*e*
			Phe(N)−Met(C^X)[h]	several angles	*f*
Leu	ψ	−40	N−C−C−N		*d*
			H−N[$i+1$]−C^{α}−H	ω	*d*
			H−N−N[$i+1$]−H	ϕ, ω	*e*
			Phe(N)−Met(C^X)[h]	several angles	*f*
Leu	$\chi1$	−59	H−C^{α}−C^{β}−H_2		*g*
			H−N−C^{β}−H_2	f	*d*
			Leu(N)−Leu($C^{\delta2}$)	$\chi2$	*f*
Phe	ϕ	−166	H−N−C^{α}−H		*d*
			H−N−C^{β}−H_2	$\chi1$	*d*
Phe	$\chi1$	56	H−C^{α}−C^{β}−H_2		*g*
			H−N−C^{β}−H_2	ϕ	*d*

[a] The MLF peptide structure calculation combines data from four 3D torsion angle experiments ($^1H-^{15}N-^{13}C-^1H$, $^1H-^{13}C-^{13}C-^1H$, $^{15}N-^{13}C-^{13}C-^{15}N$, and $^1H-^{15}N-^{15}N-^1H$) and frequency-selective $^{15}N-^{13}C$ REDOR measurements. The complete results of the calculation have been presented elsewhere.[86] [b] Each torsion angle can be measured by multiple methods; some directly probe one torsion angle, and others depend on more than one torsion angle. [c] This column refers to torsion angles that may also contribute to the observed experimental dipolar line shape or internuclear distance. [d] Data presented in this study. [e] Reif et al. (ref 79). [f] Jaroniec et al. (ref 39). [g] Unpublished data (Rienstra et al.). [h] The distances from Phe(N) to any Met ^{13}C nucleus depend on several backbone torsion angles.

overlapping solutions from multiple torsion angle data sets are likely to correspond to the correct conformation. A summary of all of the types of torsion angle measurements thus far made in MLF, and the manner in which the measurements couple to each other, is presented in Table 9. We have presented the full structure determination for MLF elsewhere.[86]

V. Conclusions

We have presented a general method for extracting ϕ, $\chi1$, and ψ torsion angle constraints from MAS spectra of solid peptides, using 3D $^1H-^{15}N-^{13}C-^1H$ dipolar chemical shift data. High-sensitivity chemical shift correlations between ^{15}N and ^{13}C nuclei were generated by amplitude-ramped SPECIFIC CP.[26] The T-MREV sequence[55] was used to recouple $^1H-^{13}C$ and $^1H-^{15}N$ interactions at relatively high MAS rates, enabling precise dipolar field measurements in U-^{13}C,^{15}N samples. This experiment exploits chemical shifts (amide ^{15}N, $^{13}C^{\alpha}$, $^{13}C^{\beta}$) that are most likely to be resolved (within and between residue types) in solid peptides and proteins,[23,24,28] and therefore may significantly expand the potential range of applications for torsion angle experiments.

Both random and systematic errors have been analyzed in detail. In this study, random errors were minimal for several reasons. First, the overall sensitivity of the direct dimension chemical shift spectra was excellent (in most cases ∼1000:1); the 2D $^{15}N-^{13}C$ spectra retained this sensitivity because of high $^{15}N-^{13}C$ polarization transfer efficiency. Second, T-MREV recoupling provided a large dynamic range in the dipolar spectra because the dephasing is γ-encoded, and the effective Hamiltonian is purely transverse (avoiding the deleterious effects of tilted axis precession, specifically zero-frequency artifacts that obscure the low-frequency features of the dipolar line shapes).[55] Third, low-frequency features in the dipolar spectra (both the controls and torsion angle experiments) could be simulated precisely by incorporation of all protons within ∼2.5 Å of each X nucleus, and modeling the relaxation with a differential ALT model allowed extremely precise (<1.0% RMSD) fits of these spectra. Finally, doubling the ratio of $^1H-^{15}N$ to $^1H-^{13}C$

evolution,[51] by proportionally incrementing the respective T-MREV periods, yielded approximately a factor of 2 improvement in precision. The overall random error in the optimized ($r = 2$) measurements of ϕ presented here was better than $\pm 3°$ with 95% confidence ($\pm 2\sigma$), even for ϕ values 40° away from the region of optimal sensitivity. Here we analyzed only the T-MREV recoupling sequence. Several pulse sequences have recently been developed for $^1H-^{13}C$ and $^1H-^{15}N$ dipolar field measurements under high-frequency MAS conditions.[81−85] One of these methods has already been incorporated into an $^1H-^{15}N-^{13}C^{\alpha}-^1H$ experiment,[81] and the others are likely to be successful as well.

Upper bounds on the systematic errors were also determined, and methods were described to avoid accumulation of such errors. We attempted to evaluate the *worst case* scenario, to ascertain the limit of precision in torsion angle measurements. First, we found that it was essential to consider differential relaxation in the data analysis. This was true in the control experiments, where a single period of T-MREV evolution was employed (i.e., $^{13}C^1H$ and $^{15}N^1H$ dipolar spectra), in the torsion angle determination for the model system *N*-acetyl-valine. Satisfactory fits could not be obtained using models that ignored relaxation altogether, or modeled it as a single-exponential decay. These models resulted in several-fold increases in the uncertainty of the torsion angle determination, and disagreement between experiment and simulation that exceeded the random noise in our measurements by an order of magnitude (i.e, ∼5−10% RMSD). Second, exclusion of weakly coupled protons in simulations yielded shifts of ∼1−2° per proton within 2.5 Å of the ^{13}C or ^{15}N nuclei. Third, the means of theoretically describing the $^{15}N-^{13}C$ CP dynamics had some impact (±3−5°in the worst case) in the interpretation of $^{15}N[i]^1H-^{13}C^{\beta}[i]^1H_2$ and $^{15}N[i+1]^1H-^{13}C^{\alpha}[i]^1H$ spectra to extract $\phi/\chi 1$ and ψ values; the anisotropy of the transfer and presence of competing polarization transfer pathways should be explicitly evaluated when possible. For the $^{15}N[i]^1H-^{13}C^{\alpha}[i]^1H$ data, the polarization transfer model had relatively little consequence. Altogether, the systematic effects may approach 10° in the worst case; however, the majority of this error can be avoided by proper modeling of the relaxation. We would recommend for future studies, in particular those involving larger proteins where the signal-to-noise ratio and/or the number of data points in the dipolar dephasing trajectory is limited, where possible, to acquire $^{13}C^1H$ and/or $^{15}N^1H$ dipolar spectra as controls for the dipolar scaling factor and relaxation rates, or if not possible, to fit the dipolar scaling factor and relaxation rates as global parameters for the entire protein data set.

Ultimately, to test the validity of torsion angle measurements, self-consistent measurements of the same angles by multiple methods should be demonstrated. We have presented such results for the tripeptide MLF here. For example, the $^{15}N^1H-^{13}C^{\alpha}[i]^1H$ spectrum from the Met residue in MLF yields a 2-fold degenerate ϕ solution (−90° and −150°); the $^{13}C^{\alpha}[i]^1H-^{13}C^{\beta}[i]^1H_2$ $\chi 1$ solution has 4-fold degeneracy (near −80°, −40°, and ±160°). The $^{15}N^1H-^{13}C^{\beta}[i]^1H_2$ spectrum agrees only with one of these eight possibilities for (ϕ, $\chi 1$) conformation, close to (−150°, −80°). In turn, the Met ψ measurement via $^{15}N-^{13}C-^{13}C-^{15}N$ (±156.6 ± 0.6°) and $^{15}N[i+1]^1H-^{13}C^{\alpha}[i]^1H$ (most favorably 161.0 ± 3.4°, and multiple other solutions) spectra agree with only one of the possible (ϕ, ψ) solutions from the $^{15}N[i]^1H-^{15}N[i+1]^1H$ spectrum, near (−150, +160°).[79] Thus, each molecular fragment, with an inherently many-fold degenerate solution space from single torsion angle measurements, can be uniquely triangulated from a combination of 3D experiments; the measurements over multiple bonds are especially important in this process. This approach can be extended along the backbone and side chain in a general way. Therefore, we expect that a combination of 3D experiments may permit de novo determination of peptide secondary structures and potentially also refinement of global folds to high resolution. The 3D $^1H-^{15}N-^{13}C-^1H$ and $^1H-^{13}C-^{13}C-^1H$ experiments provide the foundation for such a strategy, because for most residues each experiment will provide at least two and possibly several constraints. In addition, 3D $^{15}N-^{13}C-^{13}C-^{15}N$ and $^1H-^{15}N-^{15}N-^1H$ experiments provide one additional ψ or ϕ,ψ constraint per residue; numerous additional 3D schemes can be envisioned, by which individual torsion angles can be measured with greater precision and/or with different symmetry properties. We anticipate that such experiments can be applied directly to larger U-^{13}C,^{15}N-labeled peptides and proteins, in cases where the implementation is compatible with conditions of high sensitivity and resolution required to resolve large numbers of resonances.

Acknowledgment. This research was supported by the National Institutes of Health (RR-00995, AG-14366, and GM-23403). C.M.R. was a Howard Hughes Medical Institute Predoctoral Fellow; and National Institutes of Health Postdoctoral Fellow (National Research Service Award GM-20134); M.H. acknowledges support from the Human Frontier Science Program; L.J.M. was an American Cancer Society Postdoctoral Fellow; C.P.J. is a National Science Foundation Predoctoral Fellow; B.R. was a Stipendat of the Deutsche Forschung Gemeinschaft. The authors gratefully acknowledge the superb technical assistance of Dr. David J. Ruben, Ajay Thakkar, Ron Derocher, and Peter Allen.

Supporting Information Available: Equations, figures, table, and discussion of error analysis (PDF). This material is available free of charge via the Internet at http://pubs.acs.org.

JA020802P

(81) Takegoshi, K.; Imaizumi, T.; Terao, T. *Solid State Nucl. Magn. Reson.* **2000**, *16*, 271−278.
(82) Saalwachter, K.; Graf, R.; Demco, D. E.; Spiess, H. W. *J. Magn. Reson.* **1999**, *139*, 287−301.
(83) Saalwachter, K.; Graf, R.; Spiess, H. W. *J. Magn. Reson.* **1999**, *140*, 471−476.
(84) McElheny, D.; DeVita, E.; Frydman, L. *J. Magn. Reson.* **2000**, *143*, 321−328.
(85) van Rossum, B. J.; de Groot, C. P.; Ladizhansky, V.; Vega, S.; de Groot, H. J. M. *J. Am. Chem. Soc.* **2000**, *122*, 3465−3472.
(86) Rienstra, C. M.; Tucker-Kellogg, L.; Jaroniec, C. P.; Hohwy, M.; Reif, B.; McMahon, M. T.; Tidor, B.; Lozano-Parez, T.; Griffin, R. G. *Proc. Natl. Acad. Sci. U.S.A.* **2002**, *99*, 10260−10265.

Supplement to Section III. Theoretical Background

a. Peptide Geometry

We use the convention of Spiess,[1] to describe the relative orientations of each tensor relative to a common molecular frame along the C^{α}-C^{β} bond axis:

$$\Omega^{PC}\left(C^{\alpha}-C^{\beta}\right)=(\beta,\gamma)=(0,0), \tag{S1}$$

where β and γ are the Euler angles describing the transformation from principal axis system of the dipolar tensor to the common molecular frame. The other interactions involving the C^{α} are described by:

$$\Omega^{PC}\left(C^{\alpha}-N\right)=(113,0), \tag{S2}$$

and

$$\Omega^{PC}\left(C^{\alpha}-H^{\alpha}\right)=(109.5,-60). \tag{S3}$$

Interactions involving the N and C^{β} are described by

$$\Omega^{PC}\left(N-H^{N}\right)=\begin{pmatrix}\cos^{-1}\left[0.962(-0.123+0.456\cos\varphi-0.790\sin\varphi)\right],\\ \tan^{-1}\left[\dfrac{0.953\sin(\varphi+\pi/3)}{0.278+0.186\cos\varphi-0.323\sin\varphi}\right]\end{pmatrix}, \tag{S4}$$

$$\Omega^{PC}\left(C^{\beta}-H^{\beta}\right)=\left(70.5^{\circ},\chi1-2\pi/3\right), \tag{S5}$$

and

$$\Omega^{PC}\left(C^{\beta}-H^{\beta 2}\right)=\left(70.5^{\circ},\chi1+2\pi/3\right) \tag{S6}$$

We distinguish between the generalized four-bond dihedral angle (with the notation $\Phi_{a-b-c-d}$) and interbond angle

$$\Theta_{a-b-c-d}=\cos^{-1}\frac{\left|\vec{R}_{a,b}\cdot\vec{R}_{c,d}\right|}{R_{a,b}R_{c,d}} \tag{S7}$$

where $\vec{R}_{a,b}$ is the vector between nuclei a and b, and $R_{a,b}$ the internuclear distance. Torsion angle techniques are most sensitive near conformations for which the relevant projection angle is 0° or 180°. For the ϕ measurement,

$$\Theta_{H^{N}-N-C^{\alpha}-H^{\alpha}}=\cos^{-1}\left[0.962(-0.098+0.459\cos\varphi+0.823\sin\varphi)\right], \tag{S8}$$

fulfills this condition near $\phi=-120°$. For the ψ measurement,

$$\Theta_{H^N-N[i+1]-C^\alpha-H^\alpha} = \cos^{-1}\left[0.893\left(0.114 - 0.503\cos\psi + 0.871\sin\psi\right)\right], \quad \text{(S9)}$$

implying best performance near $\psi = 120°$. The coupled $\phi/\chi1$ measurement has several regions of high sensitivity. For example, where $\phi = -150°$,

$$\Theta_{H^N-N-C^\beta-H^{\beta1}} = \cos^{-1}\left[-0.038 - 0.910\cos\chi1 - 0.220\sin\chi1\right] \quad \text{(S10)}$$

and

$$\Theta_{H^N-N-C^\beta-H^{\beta2}} = \cos^{-1}\left[-0.038 + 0.646\cos\chi1 - 0.678\sin\chi1\right] \quad \text{(S11)}$$

Thus $\Theta_{H^N-N-C^\beta-H^{\beta1}}$ is in a favorable regime near $\chi1 = 15°$ or $-165°$, and $\Theta_{H^N-N-C^\beta-H^{\beta2}}$ is favorable near $\chi1 = -45°$ or $135°$. For amino acid residues with a single H^β, the $^{15}N^1H$-$^{13}C^\beta[i]^1H$ line shapes are most sensitive to torsion angle changes near $(\phi, \chi1) = (0°, 60°)$, $(-120°, \pm180°)$, $(-170°, 20°)$, and $(45°, -140°)$. For residues with C^β methylenes, additional regions of sensitivity arise near $(\phi, \chi1) = (0°, 0°)$, $(-125°, -55°)$, $(50°, -20°)$, and $(-160°, 130°)$.

b. T-MREV Dipolar Evolution

The relaxation rates in Eq. 7 in the main text are derived by assuming that each spin state, in the absence of multiple-pulse irradiation, can be assigned a single phenomenological relaxation rate proportional to the proton coherence order. Specifically we assume, e.g.,

$$\Gamma_{Iz} = R_1 = 0, \quad \text{(S12a)}$$

$$\Gamma_{Ix} = \Gamma_{Iy} = R_2, \text{ and} \quad \text{(S12b)}$$

$$\Gamma_{Sz} = \Gamma_{Sx} = \Gamma_{Sy} = 0 \quad \text{(S13c)}$$

i.e., that the relaxation of transverse proton spin states is much greater than that of all other coherences. Likewise for multi-spin coherences, for example,

$$\Gamma_{I1xI2x} = 2R_2 \quad \text{(S13d)}$$

Now to compute the average relaxation rate of an arbitrary coherence under a multiple pulse sequence, we use first-order average Liouvillian theory,[2-5]

$$\bar{\Gamma}^{(1)}_{jk} = \frac{1}{\tau_c}\int_0^{\tau_c} \langle j|\hat{U}^\dagger_{rf}\hat{\Gamma}_{jk}\hat{U}_{rf}|k\rangle dt, \quad \text{(S14)}$$

to compute the first-order average relaxation rate under the influence of the pulse sequence described by $\hat{U}_{rf}$. We note that the $\hat{\Gamma}_{jk}$ matrix has non-zero elements only on the diagonal. Now for the T-MREV sequence element,

$$\tau_{90}(\bar{Y})-\tau_{90}-\tau_{90}(\bar{Y})-\tau_{90}(X)-\tau_{90}-\tau_{90}(X)-\tau_{90}(\bar{X})-\tau_{90}-\tau_{90}(\bar{X})-\tau_{90}(Y)-\tau_{90}-\tau_{90}(Y) \quad \text{(S15)}$$

where $\tau_{90}=\frac{1}{4}\frac{2\pi}{\omega_{1H}}$, we can evaluate effective relaxation for the initial coherence

$$\left|2S_Y I_\psi\right\rangle=\left|2S_Y I_X\right\rangle\cos\psi+\left|2S_Y I_Y\right\rangle\sin\psi \quad \text{(S16)}$$

by setting $\psi=0$ (it can easily be demonstrated that the result is independent of ψ) and computing the first half of the reflection symmetric sequence ($\tau_c=6\tau_{90}$) as

$$\bar{\Gamma}^{(1)}_{jk}=\frac{1}{\tau_c}\int_0^{\tau_c}\left\langle j\left|\hat{U}^{\dagger}_{rf}\hat{\Gamma}_{jk}\hat{U}_{rf}\right|k\right\rangle dt=$$

$$\frac{1}{\tau_c}\begin{bmatrix}\int_0^{3\tau_{90}}\Gamma_{2S_Y I_X}\,dt+\\ \int_0^{\tau_{90}}\left(\Gamma_{2S_Y I_X}\sin^2\left(\frac{t\pi}{2\tau_{90}}\right)+\Gamma_{2S_Y I_Z}\cos^2\left(\frac{t\pi}{2\tau_{90}}\right)\right)dt+\\ \int_0^{\tau_{90}}\Gamma_{2S_Y I_Z}\,dt+\\ \int_0^{\tau_{90}}\left(\Gamma_{2S_Y I_X}\cos^2\left(\frac{t\pi}{2\tau_{90}}\right)+\Gamma_{2S_Y I_Z}\sin^2\left(\frac{t\pi}{2\tau_{90}}\right)\right)dt\end{bmatrix}=\frac{2}{3}\Gamma_{2S_Y I_X}=\frac{2}{3}R_2 \quad \text{(S17)}$$

Likewise the relaxation rate for the coherences involving two protons can be computed as:

$$\overline{\Gamma}^{(1)}_{jk} = \frac{1}{\tau_c}\int_0^{\tau_c} \langle j|\hat{U}^{\dagger}_{rf}\hat{\Gamma}_{jk}\hat{U}_{rf}|k\rangle dt =$$

$$\frac{1}{\tau_c}\left[\begin{array}{l} \int_0^{3\tau_{90}} \Gamma_{4S_xI_{1x}I_{2x}}\, dt + \\ \int_0^{\tau_{90}} \left(\Gamma_{4S_xI_{1x}I_{2x}} \sin^4\left(\frac{t\pi}{2\tau_{90}}\right) + \Gamma_{4S_xI_{1z}I_{2z}} \cos^4\left(\frac{t\pi}{2\tau_{90}}\right)\right) dt + \\ \int_0^{\tau_{90}} \Gamma_{4S_xI_{1z}I_{2z}}\, dt + \\ \int_0^{\tau_{90}} \left(\Gamma_{4S_xI_{1x}I_{2x}} \cos^4\left(\frac{t\pi}{2\tau_{90}}\right) + \Gamma_{4S_xI_{1z}I_{2z}} \sin^4\left(\frac{t\pi}{2\tau_{90}}\right)\right) dt \end{array}\right] = \frac{9}{16}\Gamma_{4S_xI_{1x}I_{2x}} = \frac{9}{8}R_2 \qquad \text{(S18)}$$

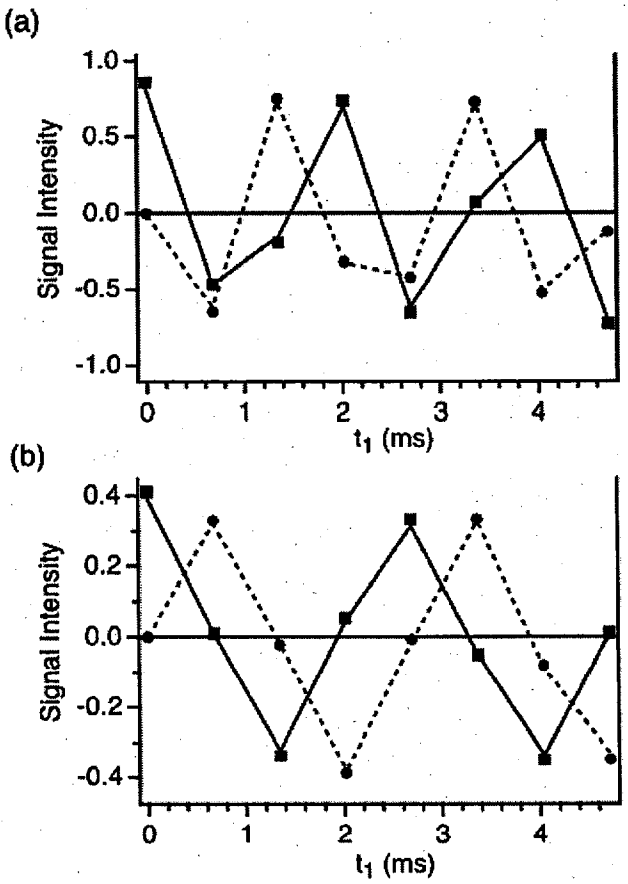

Supporting Figure 1. Fitted indirect dimension interferograms from the first 2D plane of the 3D ^{1}H-^{15}N-^{13}C-^{1}H data set. (a) Intensity modulation of the Phe $^{13}C^{\alpha}$ resonance in the direct dimension; the solid and dotted lines are the real and imaginary experimental data, respectively, and th^{e} solid squares and circles are the simulated points. (b) Intensity modulation of the Met $^{13}C^{\beta}$ resonance. In each case, 16 data points (8 complex points) are used to extract 3 intensities (Met, Leu, and Phe ^{15}N), based upon frequencies and line widths determined in control experiments.

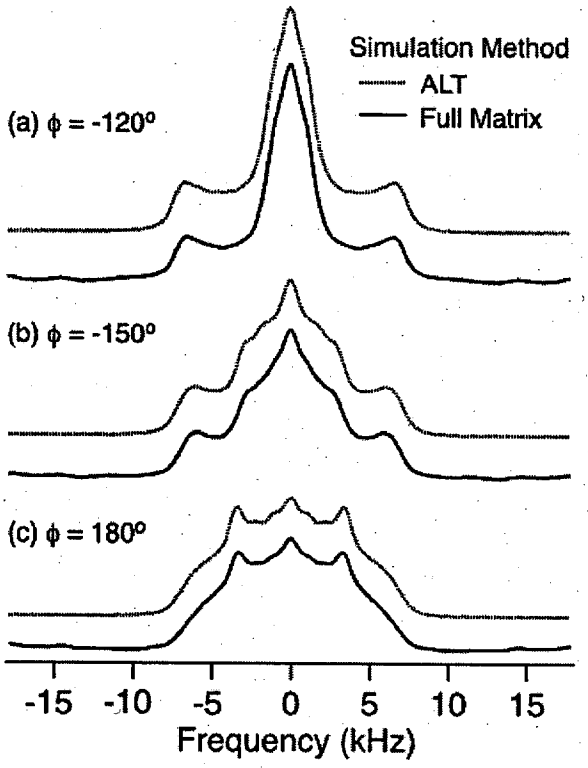

Supporting Figure 2. Simulations illustrating approaches to determine ϕ from $^{15}N^{1}H$-$^{13}C^{\alpha}[i]^{1}H$ spectra. The line shapes compare the full matrix (dotted lines) and ALT (solid lines) simulations of $^{15}N^{1}H$-$^{13}C^{\alpha}[i]^{1}H$ spectra. In all cases $\omega_r / 2\pi$ = 8.9 kHz and $\omega_{1H} / 2\pi$ = 106.8 kHz were assumed in the full matrix simulation (T-MREV-4 cycle time of 112.32 μsec), with a proton coherence relaxation rate (R_2) of 2.5 ms^{-1} and torsion angle ϕ of (a) –120°, (b) –150°, or (c) –180°. The solid lines correspond to the approximation of the first-order T-MREV average Liouvillian (see text), modeled assuming phenomenological damping of proton coherences, as described in the text. Agreement was within ±1°, with small shifts in the fitted scaling factor κ and relaxation rate Γ_2, due to the convergence properties of the ALT simulations, as shown in **Table 1**. The spectra illustrate both the substantial changes observed as a function of angle, and the excellent agreement of full matrix and ALT simulation procedures as described in **Section III.** We have compared simulation methods over the full range of ϕ values, and find in all cases that the agreement between ALT and full matrix methods is better than ±1°. The three examples presented here represent approximately the most sensitive (–120°) and least sensitive (±180°) torsion angle regimes, and in all cases the deviation over ±8 kHz is less than 0.5% (RMSD).

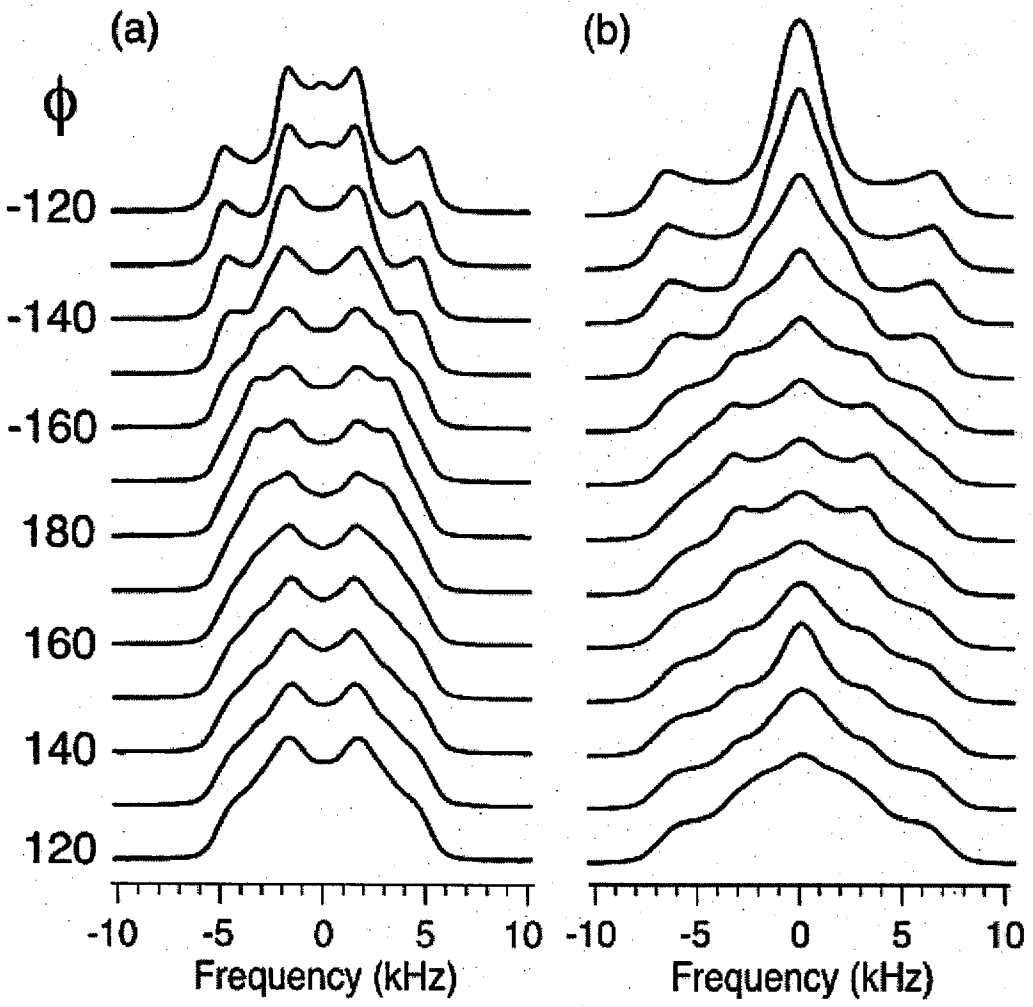

Supporting Figure 3. Simulated $^{15}N^{1}H$-$^{13}C^{\alpha}[i]^{1}H$ spectra as a function of ϕ for the (a) $r = 1$ and (b) $r = 2$ versions of the experiment. In all cases the evolution of ^{15}N and $^{13}C^{\alpha}$ transverse coherence is computed assuming the influence of both the $^{1}H^{N}$ and $^{1}H^{\alpha}$, and an analytical ^{15}N-$^{13}C^{\alpha}$ polarization transfer function. The average rate of proton coherence decay $\Gamma_2 = 2.5$ ms^{-1}.

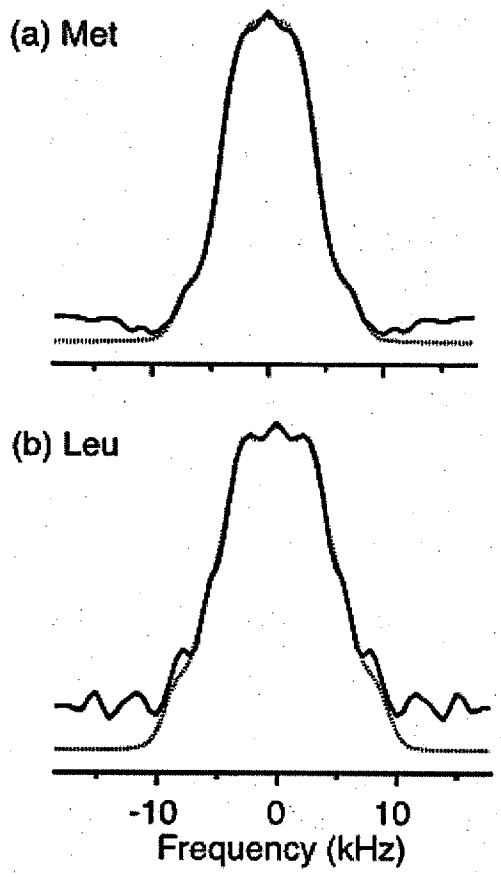

Supporting Figure 4. Experimental (solid lines) and best fit simulated (dotted lines) $^{15}N^{1}H$-$^{13}C^{\beta}[i]^{1}H$ dipolar line shapes. (a) Met, corresponding to the conformation (ϕ, $\chi1$) = (–150°, –80°) (b) Leu, corresponding to the conformation (–90°, –60°). The results are self-consistent with ϕ and $\chi1$ measurements from $^{15}N^{1}H$-$^{13}C^{\alpha}[i]^{1}H$ and $^{13}C^{\alpha}[i]^{1}H$-$^{13}C^{\beta}[i]^{1}H_2$ spectra, as described in the text.

Supporting Table 1. Systematic Shifts in ϕ Measurements, ^{15}N-Acetyl-Valine and Phe of MLF.[a]

Δ(κ) (%)	Δ(Γ_2) (%)	NAV Δ(ϕ) (°)[b]	RMSD(%) (NAV)	Phe Δ(ϕ) (°)[c]	RMSD(%) (Phe)
–10	–	–3.0	3.2	–7.2	2.5
–5	–	–1.7	2.2	–2.4	1.6
+5	–	+2.0	1.4	+1.1	1.3
+10	–	+4.2	1.7	+3.1	1.6
–[b]	–100	–5.9	6.1	–6.8	5.6
–	–50	–3.3	2.3	–1.6	2.5
–	+50	+1.8	1.3	+1.5	1.3
–	+100	+3.3	1.6	+1.3	1.7
+5	+50[c]	+2.3	1.4	+1.0	1.3
–5	+50	+0.2	2.6	–1.9	2.3
+5	–50	+1.2	3.1	–1.8	2.4

[a]The systematic errors due to large uncertainties in the scaling factor (κ) or relaxation rate (Γ_2) were evaluated by assuming incorrect values for one or both of these parameters (deviating from the optimal value), and then refitting the experimental data. A dash in column one or two indicates that the parameter was re-optimized along with the value for ϕ. The range of error assumed for each parameter is 2 to 10 times greater than the error determined from control experiments. Simulations include three protons during each T-MREV period. [b]Relative to the best fit result of -143.3°. [d]Relative to the best fit result of -162.0° (in the 2D experiments).

Discussion of Supporting Table 1.

We have considered two systematic effects, using the Phe ^{15}N^{1}H-^{13}C$^{\alpha}$[i]^{1}H spectra since the ϕ value is *ca.* 40-45° away from the region of optimal sensitivity in (ϕ = –120°), and would therefore be expected to have relatively large dependence on systematic errors. Systematic errors may arise from misset rf amplitude and/or rf inhomogeneity; covariance among the relaxation, scaling, and torsion angle; and variations in ^{15}N-^{13}C CP contact time and/or ramp profile. First, we find for Phe that experimentally mis-setting the proton rf field (ω_{1H} / 2π) amplitude by ±5%, and permitting κ to be optimized in simulation, results in a small systematic change in κ, but less than 0.5° deviation in the fitted ϕ angle. However, if κ is *fixed* in simulation to 5% below the optimal value, the value of ϕ shifts (**Table 1**) by –2.5° (to –164.4°). These results reflect the fact that an incorrect assumption about the scaling factor will lead to a systematic variation in the torsion angle determination. If the assumed scaling factor for

simulations does not agree with the effective scaling in the 3D experiment, relatively poor agreement will be achieved between experiment and simulation; the torsion angle value will be systematically incorrect and the uncertainty of the measurement *over*estimated. If the assumed scaling factor agrees with the effective value, the torsion angle will be correct but the uncertainty of the measurement *under*estimated. There are several reasons that the observed scaling factor in a 3D experiment might differ slightly from those observed in control experiments on model compounds, or even 1D or 2D control experiments on the same compound. Practical sources include long-term rf field fluctuations, and differences in rf fields as a function of sample position in the coil and/or dielectric loading effects. In addition, various sites throughout the protein may experience differing degrees of librational motion, thus altering the effective averaged dipolar coupling at each site. Finally, depending on the details of the polarization transfer method used, the transfer step may select for portions of the sample volume with higher rf fields than the average. For all of these reasons, we choose to fit the scaling factor along with angle and relaxation parameter directly from the correlated line shapes.

Similarly, the best fit ϕ value depended on the relaxation parameter Γ_2. For example, if Γ_2 is fixed in simulation to an incorrect value, 50% greater or less than the best fit value, the Phe ϕ result shifts by *ca.* ±2°. Thus the torsion angle value has a weak, but not negligible, dependence on Γ_2. If relaxation is completely ignored (i.e., $\Delta(\Gamma_2) = -100\%$), the ϕ result changes by several degrees and the quality of fit is greatly compromised. To avoid this relatively large error, differential relaxation of the coherences involving protons must be considered in the simulations. Fortunately, however, the ϕ results were not extremely sensitive to the exact value of the relaxation parameter. Therefore we expect that the strategy of assuming relaxation parameters for entire sets of resonance types (e.g., NH, CH, CH_2) may be acceptable in cases where site-resolved experimental controls may not be available, such as in larger proteins.

References

(1) Spiess, H. W. In *NMR Basic Principles and Progress*; Diehl, P., Fluck, E., Kosfeld, E., Eds.; Springer: Berlin, 1978; Vol. 15, pp 58-214.

(2) Griesinger, C.; Ernst, R. R. *Chem. Phys. Lett.* **1988**, *152*, 239-247.

(3) Levitt, M. H.; Dibari, L. *Phys. Rev. Lett.* **1992**, *69*, 3124-3127.

(4) Helmle, M.; Lee, Y. K.; Verdegem, P. J. E.; Feng, X.; Karlsson, T.; Lugtenburg, J.; de Groot, H. J. M.; Levitt, M. H. *J. Magn. Reson.* **1999**, *140*, 379-403.

(5) Ghose, R. *Concepts Magn. Reson.* **2000**, *12*, 152-172.